THESIS FOR THE DEGREE OF LICENTIATE OF ENGINEERING

Hot-carrier generation and strong coupling in metal nanoparticles

Jakub Fojt

Department of Physics
CHALMERS UNIVERSITY OF TECHNOLOGY
Göteborg, Sweden 2023

Hot-carrier generation and strong coupling in metal nanoparticles
Jakub Fojt

Department of Physics
Chalmers University of Technology
se-412 96 Göteborg, Sweden
Telephone +46 (0)31 772 10 00

Cover: Illustration of electron transfer between a nanoparticle and molecule, and of strong coupling between nanoparticles and a molecule.

Chalmers digitaltryck
Göteborg, Sweden 2023

Hot-carrier generation and strong coupling in metal nanoparticles

Jakub Fojt
Department of Physics
Chalmers University of Technology

Abstract

Metal nanoparticles are an emerging platform for energy applications such as photovoltaics, solar-to-fuel conversion and photocatalysis. Nanoparticles confine the oscillating electromagnetic field of visible light to very small volumes, which allows for efficient absorption and scattering of light in the solar spectral range.

The first part of this thesis concerns the formation of so-called hot carriers, which are highly energetic charge carriers that can be generated via the absorption of light and can drive processes relevant for energy applications. The exact mechanisms leading to the formation and transfer of hot carriers are, however, not fully understood, which hinders rational design of nanoparticles for these applications. Here, I have modeled the generation of hot carriers across nanoparticle-molecule junctions by time-dependent density functional theory calculations. I show the importance of energetic alignment between the frontier orbitals, the states in the nanoparticle, and the photon energy for the hot-carrier distribution, leading to a non-monotonic distance dependence.

The second part of this thesis focuses on modeling hybrid light-matter states. Hybrid light-matter states can form due the resonant interaction between light and electronic excitations, in a regime of light-matter interaction known as strong coupling. Common approaches for modeling strong coupling are usually limited to highly simplified descriptions of matter. Here, I derive a computationally efficient model based on dipolar coupling. A detailed description of the matter is retained by obtaining polarizabilities of components from time-dependent density functional theory. Finally, I show that the model accurately captures strong coupling behavior in nanoparticle-molecules assemblies.

Keywords: nanoparticles, strong coupling, hot carriers, nanoplasmonics

LIST OF APPENDED PAPERS

This thesis is based on work presented in the following papers:

I **Dipolar coupling of nanoparticle-molecule assemblies: An efficient approach for studying strong coupling**
Jakub Fojt, Tuomas P. Rossi, Tomasz J. Antosiewicz, Mikael Kuisma, and Paul Erhart
The Journal of Chemical Physics **154**, 094109 (2021)

II **Hot-Carrier Transfer across a Nanoparticle–Molecule Junction: The Importance of Orbital Hybridization and Level Alignment**
Jakub Fojt, Tuomas P. Rossi, Mikael Kuisma, and Paul Erhart
Nano Letters **22**, 8786-8792 (2022)

The author's contribution to the papers:

I I contributed to the implementation of the dipolar-coupling code, carried out the calculations, prepared the figures, and contributed to the writing of the paper.

II I improved the tools used for post-processing and analysis the TDDFT outputs, performed the DFT and TDDFT calculations, prepared the figures and wrote the paper.

Contents

List of abbreviations **ix**

1 Introduction **1**
1.1 Nanoparticles interacting with light 1
1.2 Strong coupling 2
1.3 Fundamental questions 2
1.4 Structure of thesis 3

2 Computational methods **5**
2.1 Continuum matter electrodynamics 5
2.1.1 Dipole expansion of the electric field 7
2.2 Density functional theory 8
2.2.1 Kohn-Sham density functional theory 9
2.2.2 The exchange-correlation functional 10
2.3 Time-dependent density functional theory 11
2.3.1 Adiabatic approximation 12
2.3.2 In the linear response regime 12

3 The localized surface plasmon in metal nanoparticles **15**
3.1 The bulk plasmon 15
3.2 The localized surface plasmon 16
3.2.1 Effect of composition and shape 17
3.2.2 Effect of non-locality 18
3.2.3 Quantum matter description 18

4 Hot-carrier generation and transfer **19**
4.1 The time scales of hot-carrier generation 19
4.2 Direct versus indirect hot-carrier transfer 20
4.3 Handles for tuning direct transfer 21

5 Strong coupling **25**

5.1 Characteristics of strong coupling 25
5.2 Coupled harmonic oscillators 26
5.3 Dipolar coupling 30

6 Summary of papers **35**

7 Conclusions and outlook **39**
7.1 Limitations 40
7.2 Outlook 41

Acknowledgments **43**

Bibliography **45**

Papers I–II **53**

List of abbreviations

DC dipolar coupling. 30–33, 35, 36, 40

DF dielectric function. 6, 15–18

DFT density-functional theory. 5, 9, 11, 40

DHCT direct hot-carrier transfer. 21–23, 39

EM electromagnetic. 2, 19, 25, 26, 40

GGA generalized-gradient approximation. 11

GLLB Gritsenko-van Leeuwen-van Lenthe-Baerends. 11

GLLB-sc Gritsenko-van Leeuwen-van Lenthe-Baerends-solid-correlation. 10, 11, 18

HC hot carrier. 1–3, 5, 11, 14, 15, 18–22, 37–41

HE hot electron. 20, 22–24, 37, 39

HH hot hole. 20, 23, 37–39

HOMO highest occupied molecular orbital. 23, 38, 39

KS Kohn-Sham. 10–13, 18, 37, 38

KS-DFT Kohn-Sham DFT. 9, 10, 22

LP lower polariton. 25, 32, 36

LSP localized surface plasmon. 1, 2, 15, 16, 18, 19, 21–23, 26, 31, 32, 37–40

LSPR localized surface plasmon resonance. 3, 17, 18, 24, 39

LUMO lowest unoccupied molecular orbital. 22, 23, 37, 39

NP nanoparticle. 1–3, 5, 15, 17–24, 30–33, 35–37, 39, 40

PDOS projected density of states. 22, 23

RT-TDDFT real-time time-dependent density functional theory. 12, 13, 18, 19, 22, 37, 40

SC strong coupling. 2, 3, 15, 25, 26, 29, 30, 32, 33, 36, 39, 40

TDDFT time-dependent density-functional theory. 5, 11, 12, 15, 18, 30, 32, 33, 35, 36, 40, 41

UP upper polariton. 25, 36

XC exchange-correlation. 10–12, 18, 31, 40, 41

1 Introduction

We are constantly in pursuit of new materials for energy applications [1–3]. Considering the climate crisis [4], it is highly relevant to search for materials that are better at producing clean energy and using energy more efficiently in industry. The challenge is understanding the connection between the atomic structure of a material and its properties. While there are only a hundred or so elements in the periodic table, the possibilities of combining them are endless, and differences at the nanoscale in a material can have a large impact on the properties of the material.

The focus of this thesis is the interaction of light and matter in nanoparticles (NPs) and their vicinity. NPs are efficient absorbers and scatterers of light [5], and have been shown to be useful for several energy applications. These include light-harvesting [6], solar-to-chemical energy conversion [7–10] and photocatalysis [11–13]. These processes are thought to occur through a mechanism where hot carriers (HCs), i.e., highly non-thermal "energetic" electrons or holes, generated through the interaction of the NP with light, give rise to a photocurrent (in light harvesting) or catalyze a chemical reaction (in solar-to-chemical energy conversion or photocatalysis).

1.1 Nanoparticles interacting with light

NPs range between a few and a few hundred nanometers in size. Already the lack of similar words for microparticles or milliparticles reveals that NPs differ drastically from larger particles. Indeed, because NPs are smaller than the wavelength of visible or near ultraviolet (UV) light, they support a mode of collective electronic excitation called the localized surface plasmon (LSP). This is described in Chapter 3 of this thesis. The dephasing of this mode gives rise to HCs that can be used for energy applications.

The material properties required to create a photocurrent, or to catalyze a particular chemical reaction, differ depending on the specific photovoltaic device or reaction in question. The properties of NPs depend on tunable parameters including size, shape, and composition. Hence, NPs can be tailored to desired applications. The dependence of NP properties on size, shape and composition is explored in Chapters 3 and 4.

Today, experimentalists routinely manufacture NPs with precise control over the outcome [14, 15]. The preference for different facets to form can be controlled, resulting in spherical, ellipsoidal, cube, or rod-like shapes, in sizes from 5 nm upwards [14, 15]. Alloyed NPs can be made in disordered [16] or ordered structures, e.g., with an inner core and outer shell of different materials [17], or even multi-shell structures with smaller NPs deposited on the outermost surface [18].

1.2 Strong coupling

The coupling strength of the interaction between light and matter can be modified by confining the electromagnetic (EM) field to a smaller volume, i.e., a cavity. An increased coupling strength of an EM mode to an electronic transition results in faster exchange of energy between the EM field and electronic state. For weak coupling strengths, this means that if light previously induced an electronic transition in the material, the confined light will now induce the same transition at a higher rate. In the regime of strong coupling (SC), however, energy is coherently exchanged between the EM field and the material, and hybrid states of light and matter form, that have different eigenenergies than the underlying EM mode and electronic state(s) [19]. This phenomenon has been demonstrated to be useful in modifying chemical reaction rates [20]. NPs are a suitable platform to exploit SC, as the LSP has the same ability to confine the EM field as traditional cavities. Modeling SC is the topic of Chapter 5.

1.3 Fundamental questions

Questions that this thesis aims to answer are:

- What determines the efficiency of HC transfer from NPs to molecules?
- To what extent is SC in NP-molecule assemblies captured by dipolar coupling?

The answer to the first question would indicate which parameters can be tuned to achieve higher efficiencies in HC devices. The second question pertains to the issue that ab initio methods are computationally expensive, and NPs larger than a few nanometers are practically impossible to model. In real devices, one could, however, expect to have larger

NPs, the involvement of many NPs or of many molecules. To bridge the size gap between experiment and theory, methods that are cheaper at the expense of accuracy can be appropriate, as long as the limits of their accuracy are known.

1.4 Structure of thesis

The remainder of this thesis is structured as follows. In Chapter 2, the theoretical foundation that I have used to model light-matter interactions is presented together with the computational methods. The following chapters cover the central topics of this thesis. The optical properties of NPs and the localized surface plasmon resonance (LSPR) are covered in Chapter 3. HC generation and transfer are covered in Chapter 4 and SC in Chapter 5. In Chapter 6, the two papers that serve as the basis of this thesis are summarized. Lastly, in Chapter 7, we return to the main questions of this thesis, discussing possible answers in the context of energy applications.

2 Computational methods

This chapter reviews the theory of light-matter interaction, which forms the basis of the used computational methods. The description of light is at the level of classical electrodynamics, and the matter is described with either continuum or quantum models. First I review continuum matter electrodynamics, that I use to calculate absorption spectra of NPs in Chapter 3 and of NP-molecule ensembles in Chapter 5. Then I present density-functional theory (DFT) and time-dependent density-functional theory (TDDFT), i.e., quantum theories for electrons, which I use to (again) compute absorption spectra of NPs in Chapter 3 and to compute probabilities of HC formation in Chapter 4.

In practice to perform DFT and TDDFT calculations, I use the GPAW [21–26], ASE [27] and VASP [28–31] codes.

2.1 Continuum matter electrodynamics

Classical electrodynamics with a continuum description of matter describes the light-matter interaction in susceptibilities of materials: linear functions that tell how the material changes, e.g., its charge distribution in response to an electric field. It does not matter for the theory what the functional forms of the susceptibilities are, and for practical calculations we can obtain them from other levels of theory, experiment or as simple phenomenological models. The review of classical electrodynamics in this section follows Griffiths [32, Chapter 4].

Gauss's law relates the charge distribution in space $\rho(\boldsymbol{r})$ to the electric field

$$\varepsilon_0 \nabla \cdot \boldsymbol{E}(\boldsymbol{r}) = \rho(\boldsymbol{r}), \tag{2.1}$$

where ε_0 is the free-space permittivity. The charge distribution is exactly zero in vacuum. In a material, charge can be redistributed due to electric fields, as a so-called

bound charge density

$$\rho(\boldsymbol{r}) = \begin{cases} 0, & \boldsymbol{r} \text{ in vacuum} \\ -\nabla \cdot \boldsymbol{P}(\boldsymbol{r}), & \boldsymbol{r} \text{ in a material.} \end{cases} \tag{2.2}$$

The quantity $\boldsymbol{P}(\boldsymbol{r})$ is called polarization and is zero in vacuum. Thus we write for all space (dropping the explicit $(\boldsymbol{r})$ from the notation)

$$\nabla \cdot (\varepsilon_0 \boldsymbol{E} + \boldsymbol{P}) = 0. \tag{2.3}$$

For convenience, we call the quantity inside the bracket in Eq. (2.3) the *displacement field* $\boldsymbol{D}$ and introduce the dielectric function (DF) $\varepsilon = (1 + \chi_e)$. The latter is a materials property that tells us how the material is polarized in response to an electric field

$$\boldsymbol{P} = \varepsilon_0 \chi_e \boldsymbol{E}. \tag{2.4}$$

Putting it all together, the displacement field

$$\boldsymbol{D} = \varepsilon_0 \varepsilon \boldsymbol{E} \tag{2.5}$$

is used to express Gauss's law in the convenient form

$$\nabla \cdot \boldsymbol{D} = 0. \tag{2.6}$$

To describe time-dependent fields (light) we need to consider that the dielectric function can in principle be an operator in the form of a convolution over the electric field at all previous times (we restrict the discussion to isotropic DFs that are local in space and linear in frequency) [33, Chapter 9]. Hence, a description in the time domain is unnecessarily complicated, and we instead express Gauss's law in frequency space.

Gauss's law is the fundamental equation for the electric field

$$\nabla \cdot \boldsymbol{D}(\omega) = 0 \tag{2.7}$$

$$\boldsymbol{D}(\omega) = \varepsilon_0 \varepsilon(\omega) \boldsymbol{E}(\omega). \tag{2.8}$$

Here, the dependence on fields on $\boldsymbol{r}$ is implied, and the geometry of materials encoded in the $\boldsymbol{r}$-dependence of the DF $\varepsilon(\omega)$.

The frequency dependent $\boldsymbol{E}(\omega)$ and $\boldsymbol{D}(\omega)$ are Fourier components of the corresponding time-dependent quantities, and are related through the Fourier transform. We can interpret each Fourier component at frequency ω, as a time dependent wave traveling as

$$\boldsymbol{E}(t) = \mathrm{Re}[\boldsymbol{E}(\omega) \mathrm{e}^{-i\omega t}]. \tag{2.9}$$

2.1.1 Dipole expansion of the electric field

For certain charge distributions the electric field has a very simple form. A point charge q at the origin in vacuum has exactly the electric field [32, Chapter 3]

$$\boldsymbol{E} = \frac{q}{4\pi\varepsilon_0}\frac{\hat{r}}{r^2}, \tag{2.10}$$

where $r = |\boldsymbol{r}|$ is the norm of the position vector and $\hat{r} = \boldsymbol{r}/r$ its unitless direction. For arbitrary charge distributions $\rho(\boldsymbol{r})$ the expression for the field can be complicated, but can always be expanded in a series in powers of $1/r$

$$\boldsymbol{E} = \frac{1}{4\pi\varepsilon_0}\left[\frac{q}{r^2}\hat{r} + \frac{1}{r^3}\left[3(\boldsymbol{d}\cdot\hat{r})\hat{r} - \boldsymbol{d}\right] + \ldots\right], \tag{2.11}$$

where the charge q and dipole moment $\boldsymbol{d}$ are obtained from the charge density

$$q = \int \rho(\boldsymbol{r})\mathrm{d}\boldsymbol{r} \tag{2.12}$$

$$\boldsymbol{d} = \int \rho(\boldsymbol{r})\boldsymbol{r}\mathrm{d}\boldsymbol{r}. \tag{2.13}$$

The lowest terms in Eq. (2.11) (point charge term $1/r^2$ and dipole term $1/r^3$) dominate at large distances from the charge distribution. This turns out to be useful, because far from any localized charge distribution, i.e., any material, the field can be approximated as the field from a charged dipole (Fig. 2.1); the interaction of the material being encoded in its charge and dipole moment. For a charge neutral material ($q = 0$), the dipole moment is independent of the choice of coordinate system. Using matrix algebra for the vectors ($\boldsymbol{r}$ is a one-column matrix, $\boldsymbol{r}^{\mathrm{T}}$ its transpose, $\boldsymbol{r}^{\mathrm{T}}\boldsymbol{r}'$ an inner product and $\boldsymbol{r}(\boldsymbol{r}')^{\mathrm{T}}$ an outer product), we realize that the field of a dipole is linear in the dipole moment

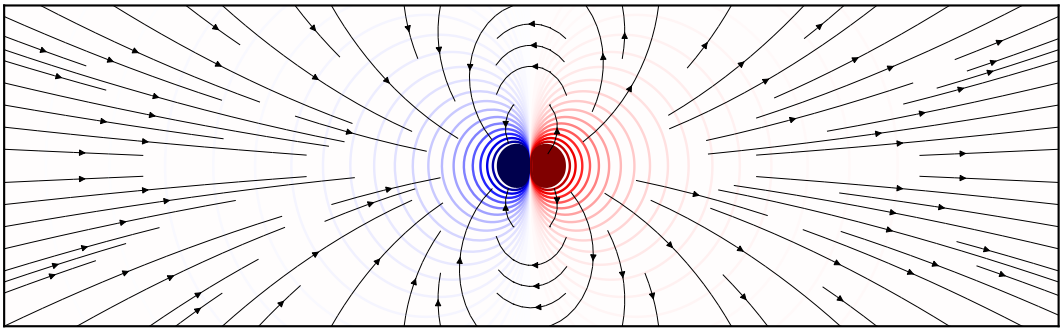

Figure 2.1: Electric field lines and potential isolines for a point dipole.

(position and frequency dependence is implied)

$$\boldsymbol{E}_{\text{dipole}} = \frac{1}{4\pi\varepsilon_0}\left[\frac{3\boldsymbol{r}\boldsymbol{r}^{\mathrm{T}}}{r^5} - \frac{1}{r^3}\right]\boldsymbol{d}. \tag{2.14}$$

For wavelengths larger than the objects in our system, the field is approximately constant over each object, and we commonly assume a linear relationship to the dipole moment of the object

$$\boldsymbol{d}(\omega) = \boldsymbol{d}_{\text{perm}} + \boldsymbol{\alpha}(\omega)\boldsymbol{E}(\omega), \tag{2.15}$$

where $\boldsymbol{d}_{\text{perm}}$ is a permanent dipole moment. The *polarizability* $\boldsymbol{\alpha}(\omega)$ is in general a tensor of rank two, so that a field in one direction can induce a dipole in another direction. When the response is isotropic, however, $\alpha(\omega)$ can be treated as a scalar. Viewing the small object from a sufficient distance, only the dipole radiation is significant. This leads to an expression for the energy absorbed by the object [34, Chapter 6].

For particles smaller then the wavelength of light, the absorption cross section C_{abs} that relates irradiance I to absorbed energy per unit time W_{abs}

$$W_{\text{abs}} = C_{\text{abs}} I \tag{2.16}$$

is given by

$$C_{\text{abs}}(\omega) = -\frac{2\omega}{c\varepsilon_0}\operatorname{Im}\alpha(\omega), \tag{2.17}$$

where c is the speed of light.

2.2 Density functional theory

I consider materials consisting of electrons and atomic nuclei in the Born-Oppenheimer approximation [35]. This means that at any given time, the nuclei are regarded frozen in some geometrical configuration, and the electrons perfectly adapted to that configuration — a good approximation in many cases [36, Chapter 3]. In the remainder of this chapter, I use Hartree atomic units $e = \hbar = 4\pi\varepsilon_0 = 1$ for simplicity.

Electrons obey the Schrödinger equation

$$\hat{H}\Psi_I = E_I\Psi_I, \tag{2.18}$$

where the Hamiltonian $\hat{H}$ encodes the kind of material through the *external potential*, i.e., the Coulomb attraction of electrons to the charged atomic nuclei. Unfortunately, the Schrödinger equation is practically not solvable if the material of interest consists of more than a few electrons, because the many-body wave functions Ψ_I are functions of the coordinates of all electrons. Any numerical discretization scheme requires storing

and operating on P^{3N} coefficients, P being the number of parameters per dimension (10 would be an extremely optimistic estimate) and N the number of electrons. Clearly, this is impossible for more a few electrons, a notion known as the exponential wall [37].

One strategy in electronic structure theory is to reformulate the Schrödinger equation into a form where only the density of electrons

$$\rho_I(\boldsymbol{r}) = \int |\Psi_I(\boldsymbol{r}, \boldsymbol{r}_2, \dots, \boldsymbol{r}_N)|^2 \mathrm{d}\boldsymbol{r}_2 \dots \mathrm{d}\boldsymbol{r}_N \tag{2.19}$$

appears (note that in the previous section ρ denotes *charge* density), and eventually introduce approximations making it computationally tractable. DFT is based on the two Hohenberg-Kohn theorems [38]:

1. There is a one-to-one correspondence of the external potential experienced by the electronic system and its ground state electronic density $\rho(\boldsymbol{r})$.
2. There is a universal functional for the total energy of any density $E[\rho]$, exactly equivalent to the Schrödinger equation, and the global minimum of the functional

   $$E_{\mathrm{gs}} = \min_{\rho(\boldsymbol{r})} E[\rho] \tag{2.20}$$

   is the ground state energy, and the corresponding density the ground state density.

The theorems are valid for densities that can be formed from fermionic wave functions (this property is called N-representability) and that are the ground state density of some external potential (V-representability) [36]. Compared to the Schrödinger equation, the number of numeric coefficients is reduced from P^{3N} to P^3 which makes DFT more useful for large systems, such as those encountered in materials science. However, the Hohenberg-Kohn theorems do not give the exact form of the functional form $E[\rho]$, so we have to look further for something that can actually be computed.

2.2.1 Kohn-Sham density functional theory

Kohn-Sham DFT (KS-DFT) [39] provides a tractable scheme for the evaluation of $E[\rho]$ by considering an *auxiliary*, non-explicitly-interacting system of particles instead of the true, explicitly-interacting system of particles. The auxiliary system is governed by

$$\hat{H}_{\mathrm{KS}} \psi_{n\boldsymbol{k}} = \varepsilon_{n\boldsymbol{k}} \psi_{n\boldsymbol{k}} \tag{2.21}$$

$$\hat{H}_{\mathrm{KS}} = -\frac{1}{2}\nabla^2 + V_{\mathrm{eff}}[\rho](\boldsymbol{r}) \tag{2.22}$$

$$\rho(\boldsymbol{r}) = \sum_n \sum_{\boldsymbol{k}}^{1\mathrm{BZ}} f_{n\boldsymbol{k}} \left|\psi_{n\boldsymbol{k}}(\boldsymbol{r})\right|^2, \tag{2.23}$$

where $f_{n\boldsymbol{k}}$ is the occupation number of the Kohn-Sham (KS) states. The quantum number $\boldsymbol{k}$ is defined only for extended systems and runs over the first Brillouin zone. In Eq. (2.22) $V_{\text{eff}}[\rho](\boldsymbol{r})$ is an effective potential, and the KS *ansatz* is that $V_{\text{eff}}[\rho](\boldsymbol{r})$ *can* be chosen such that the auxiliary system and the true system have then same ground state density. If the assumption holds, which has not formally been proven [36, Chapter 7], it follows from the Hohenberg-Kohn theorems that also the ground state energies of the auxiliary system and true system are the same. The strength of the KS ansatz is that Eq. (2.21) is effectively a single-particle Schrödinger equation requiring P^3 coefficients to solve. The interactions of electrons are implicitly included through the functional $V_{\text{eff}}[\rho](\boldsymbol{r})$.

An expression for $V_{\text{eff}}[\rho](\boldsymbol{r})$ is obtained by hiding the physics of interactions in the exchange-correlation (XC) energy functional $E_{\text{xc}}[\rho]$, which is formally defined as the difference between the kinetic and electron-electron interaction energies of the true and auxiliary systems [36, Chapter 7]. Its functional derivative is the XC potential functional

$$v_{\text{xc}}[\rho](\boldsymbol{r}) = \frac{\delta E_{\text{xc}}[\rho]}{\delta \rho}. \tag{2.24}$$

The XC energy and potential functionals have to be approximated for practical calculations, which I discuss in the next section.

The effective potential is comprised of the external potential, the Coulomb potential from all electrons in the auxiliary system, and the XC potential that contains everything else [36, Chapter 7]

$$V_{\text{eff}}[\rho](\boldsymbol{r}) = V_{\text{ext}}(\boldsymbol{r}) + \int \frac{\rho(\boldsymbol{r}')}{|\boldsymbol{r} - \boldsymbol{r}'|} \mathrm{d}r' + v_{\text{xc}}[\rho]. \tag{2.25}$$

The total energy functional in KS-DFT is [40, Chapter 2]

$$E[\rho] = \sum_{n} \sum_{\boldsymbol{k}}^{1\text{BZ}} f_{n\boldsymbol{k}} \varepsilon_{n\boldsymbol{k}} - \frac{1}{2} \int \frac{\rho(\boldsymbol{r})\rho(\boldsymbol{r}')}{|\boldsymbol{r} - \boldsymbol{r}'|} \mathrm{d}\boldsymbol{r}' \mathrm{d}\boldsymbol{r} + E_{\text{xc}}[\rho] - \int v_{\text{xc}}[\rho](\boldsymbol{r})\rho(\boldsymbol{r}) \mathrm{d}\boldsymbol{r}. \tag{2.26}$$

Self-consistent solutions to Eqs. (2.21-2.26) can be found numerically, *given functional forms* for the XC functional for the energy and potential and other observables of interest. Assuming validity of the KS ansatz and the exact XC functionals, this scheme is exactly equivalent to the Schrödinger equation.

2.2.2 The exchange-correlation functional

With an approximate form for the XC functional, we can readily compute electronic structures. I use the Gritsenko-van Leeuwen-van Lenthe-Baerends-solid-correlation

(GLLB-sc) XC functional [25] for calculations of plasmonic response, but it is instructive to first explain simpler forms.

The local density approximation (LDA) [41–43] is a *local* form for the XC functional, meaning that the value of the potential at every point $\boldsymbol{r}$ depends only on the density at that point. The actual form of the potential is defined to be the same as for a homogeneous electron gas of density n, where the exchange has an exact analytic expression [41, 42], and the correlation is fitted to quantum Monte Carlo calculations [43].

Generalized-gradient approximation (GGA) functionals extend the LDA to depend also on gradients of the density. There are a few different choices for the parametrization of the functional form, that satisfy different exact conditions in limiting cases [36, Chapter 8]. The Perdew-Burke-Ernzerhof (PBE) [44] functional is one such example.

Meta-GGAs try to improve on GGAs by introducing dependence on the wave functions. The Gritsenko-van Leeuwen-van Lenthe-Baerends (GLLB)[45] functional belongs to this class, and incorporates a discontinuity in the exchange-correlation potential at integer occupation numbers

$$\Delta_{\mathrm{xc}} = \lim_{\delta \to 0} v_{\mathrm{xc}}(\boldsymbol{r}, N + \delta) - v_{\mathrm{xc}}(\boldsymbol{r}, N - \delta) \neq 0 \tag{2.27}$$

which should be a feature of the true XC functional [46]. The GLLB-sc functional [25] is a modification of GLLB with better description of solids and correlation. It greatly improves the location of the d-band in noble metals, which is important for plasmonic systems composed of these metals [24, 47, 48].

2.3 Time-dependent density functional theory

Optical absorption and HC generation processes are not properties of the ground state density, and thus outside of the scope of DFT. However, TDDFT, which appears analogous to DFT, covers these excited state properties. In this section I focus on isolated systems and omit the $\boldsymbol{k}$ quantum number of KS states.

For systems much smaller than the wavelength of light, the light-matter interaction is described by a scalar time-dependent potential $V_1(t)$ [40, Chapter 3]. Any electronic excitations induced by the light are described by the time-dependent Schrödinger equation

$$i\frac{\partial}{\partial t}\Psi(t) = \left[\hat{H}_0 + V_1(t)\right]\Psi(t). \tag{2.28}$$

TDDFT is based on the Runge-Gross theorem [49] which formally proves the one-to-one correspondence between $V_1(t)$ and initial condition $\Psi(0)$ to the time-dependent electron density $\rho(\boldsymbol{r}, t)$ (defined analogously to Eq. (2.19)). The Runge-Gross theorem is thus the

time-dependent analogue of the Hohenberg-Kohn theorem. The analogy to the Kohn-Sham ansatz is the van Leeuwen theorem [50] that is valid under most reasonable circumstances [40, Chapter 3] and states that there is a time-dependent auxiliary system that gives the exact time-dependent density

$$i\frac{\partial}{\partial t}\psi_n(t) = \hat{H}_{\mathrm{KS}}\psi_n(t) \tag{2.29}$$

$$\hat{H}_{\mathrm{KS}} = -\frac{1}{2}\nabla^2 + V_{\mathrm{eff}}[\rho](\boldsymbol{r}), \tag{2.30}$$

given some initial conditions on the KS wave functions $\psi_i(\boldsymbol{r},0) = \psi_i^{(0)}(\boldsymbol{r})$. Here, the effective potential is formally a functional of the density *at all previous times* and the initial condition [40, Chapter 4]. The latter condition is formally relaxed by assuming that the potential is zero before $t = 0$; then the initial condition is that the system is in its ground state.

The numeric propagation of Eq. (2.29) and self-consistent evaluation of Eq. (2.30) at every time step defines the real-time time-dependent density functional theory (RT-TDDFT) method (in contrast to other common TDDFT schemes where the equations are essentially Fourier transformed and solved in frequency space [51]).

2.3.1 Adiabatic approximation

Often, one assumes Eq. (2.25) for the XC functional in the time-dependent case, so that only the instantaneous density determines the potential. This defines the adiabatic approximation, which is exact when the external potential varies infinitely slowly (causing the system to always be in its ground state) [40, Chapter 4]. Absorption spectra of metallic particles computed using the adiabatic approximation have been shown to be consistent with experimental spectra [52, 53], motivating its use in this thesis.

2.3.2 In the linear response regime

In the limit of weak perturbation $V_1(t)$, certain observables of the KS system are linear in the perturbation, just like the linear materials in Sect. 2.1. I will not present the proof here, instead I refer to Ref. [54, Supplementary Notes]. As an example, consider the dipole moment

$$\boldsymbol{d}(t) = -\int \rho(\boldsymbol{r},t)\boldsymbol{r}\,\mathrm{d}\boldsymbol{r}, \tag{2.31}$$

as a response to a spatially constant electric field $\boldsymbol{E}(t) = -\nabla V_1(t)$ where $V_1(t) = (k_x x + k_y y + k_z z)v(t)$. The dipole moment is linear in the perturbation and thus a polarizability

is well defined. Using the definition for polarizability Eq. (2.15)

$$[\boldsymbol{\alpha}(\omega)]_{\mu\nu} = -\frac{[\Delta\boldsymbol{d}(\omega)]_\mu}{[\boldsymbol{E}(\omega)]_\nu} = -\frac{[\Delta\boldsymbol{d}(\omega)]_\mu}{k_\nu \cdot v(\omega)}, \tag{2.32}$$

where $\Delta\boldsymbol{d}(\omega) = \boldsymbol{d}(\omega) - \boldsymbol{d}_{\text{perm}}$ and Greek subscript letters refer to Cartesian components of tensors. It is clear that we only need to save the induced dipole moment $\Delta\boldsymbol{d}(t)$ during the calculation, and Fourier transform the perturbation and the induced dipole moment, to obtain the polarizability.

We can exploit the assumption that the material is linear, to compute the dipole moment response $\Delta d'_x$ to any other weak perturbation v', as long as the Fourier spectra of v and v' are non-zero in relevant overlaps. By Eq. (2.32) (constraining ourselves to perturbations in x and response in x)

$$\Delta d'_x(\omega) = -k'_x v'(\omega) \cdot \alpha_{xx}(\omega) \tag{2.33}$$

$$= k'_x v'(\omega) \cdot \frac{\Delta d_x(\omega)}{k_x v(\omega)}. \tag{2.34}$$

Taking the inverse Fourier transform $\Delta d'_x(t)$ is obtained. Conveniently, the actual time-dependent calculation is performed with a δ-kick

$$v(t) = \delta(t) \tag{2.35}$$

that has a constant Fourier spectrum, leading to

$$\Delta d'_x(\omega) = \frac{k'_x}{k_x} v'(\omega) \cdot \Delta d_x^{(\text{kick})}(\omega). \tag{2.36}$$

A similar procedure works to obtain any other observable that is linear in the perturbation. The KS density matrix in the basis of the ground state KS orbitals

$$\rho_{nn'}(t) = \sum_k f_k \cdot \int \left(\psi_n^{(0)}(\boldsymbol{r})\right)^* \psi_k(\boldsymbol{r}, t)\mathrm{d}\boldsymbol{r} \int \psi_k^*(\boldsymbol{r}', t)\psi_{n'}^{(0)}(\boldsymbol{r}')\mathrm{d}\boldsymbol{r}'. \tag{2.37}$$

is a quantity that can be used to obtain any density-based observable, as it contains all the information about the system. The electron-hole part of the matrix $\rho_{ia}(t)$, where $f_i > f_a$, is linear in perturbation. We can perform a RT-TDDFT calculation for the δ-kick and save the electron-hole part of the induced density matrix $\Delta\rho_{ia}^{\text{kick}}(t)$ for all times. Then the response to any other weak perturbation is

$$\Delta\rho_{ia}(\omega) = \frac{k'_x}{k_x} \Delta\rho_{ia}^{\text{kick}}(\omega) v'(\omega). \tag{2.38}$$

Ultimately we want to compute HC distributions, i.e., changes in occupations, which are read out from the diagonals of $\Delta\rho_{nn'}(t)$. The diagonals are, however, quadratic in perturbation [54, Supplementary Notes]. To obtain them for any perturbation, given only the δ-kick response, we first calculate the electron-hole part of the density matrix Eq. (2.38) and then use a relation that can be derived using perturbation expansions

$$\Delta\rho_{ii'}(t) = -\sum_k \frac{\Delta\rho_{ki'}(t)}{\sqrt{f_{i'} - f_k}} \frac{\Delta\rho^*_{ki}(t)}{\sqrt{f_i - f_k}}, \text{ if } f_i = f_{i'} = 2 \tag{2.39}$$

$$\Delta\rho_{aa'}(t) = \sum_k \frac{\Delta\rho_{ka'}(t)}{\sqrt{f_k - f_{a'}}} \frac{\Delta\rho^*_{ka}(t)}{\sqrt{f_k - f_a}}, \text{ if } f_a = f_{a'} = 0. \tag{2.40}$$

3

The localized surface plasmon in metal nanoparticles

NPs interact strongly with visible or near visible light, thanks to the presence of the LSP, a mode of collective electronic motion. Traditionally, theses and textbooks on the topic describe the LSP in the framework of classical electrodynamics of continuum materials. Adhering to the tradition, this chapter begins with such a description, following Bohren [5]. This is sufficient to understand the SC of NPs and molecules that is the topic of Chapter 5. Later in this chapter, I consider a quantum description of electrons in NPs based on TDDFT. This description makes it possible to study HC generation in NPs in Chapter 4.

3.1 The bulk plasmon

The starting point in understanding the LSP from electrodynamics is to consider a related collective movement in *bulk* materials: the bulk plasmon. The fundamental equation in this context is the one for the electric field, combining Gauss's law Eq. (2.7) with the expression for the displacement field Eq. (2.8)

$$\varepsilon_0 \varepsilon(\omega) \nabla \cdot \boldsymbol{E}(\omega) = 0. \tag{3.1}$$

Consider an infinitely extended homogenous material, i.e., bulk, described by the dispersive DF $\varepsilon(\omega)$. Eq. (3.1) can always be satisfied by Fourier components of the electric field $\boldsymbol{E}(\omega)$ that are purely transversal

$$\nabla \cdot \boldsymbol{E}(\omega) = 0, \tag{3.2}$$

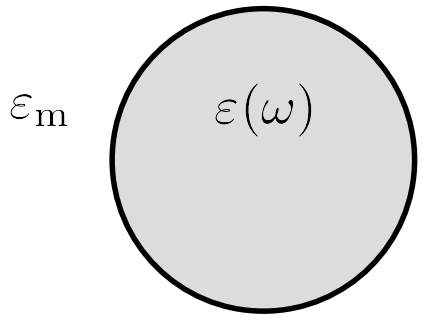

Figure 3.1: In Mie theory, the electric field for a sphere with DF $\varepsilon(\omega)$ in an environment ε_m is solved for.

corresponding to a propagating wave. However, in the special case when $\varepsilon(\omega) = 0$, a longitudinal mode $\nabla \cdot \boldsymbol{E}(\omega) \neq 0$ is allowed. This mode corresponds to the polarization of free charge in the material, i.e., a collective movement of electrons.

Do all materials support a bulk plasmon then? The answer is no, as the condition $\varepsilon(\omega) = 0$ is not so trivial to fulfill. The Drude free-electron model for the DF is one example that supports the bulk plasmon

$$\varepsilon(\omega) = 1 - \frac{\omega_p^2}{\omega^2 + i\gamma\omega}. \tag{3.3}$$

The model DF has two parameters: the *plasma* frequency ω_p and damping constant γ. At the frequency $\omega = \sqrt{\omega_p^2 - \gamma^2} \approx \omega_p$ the real part of $\varepsilon(\omega)$ is zero, allowing a bulk plasmon mode. However, as the imaginary part of $\varepsilon(\omega)$ is finite, the mode is damped and cannot sustain forever without external driving force.

3.2 The localized surface plasmon

In contrast to the bulk plasmon, the LSP forms due to a constrained geometry. In Mie theory [56] one solves Eq. (2.7) exactly for a geometry where the DF is constant outside a sphere (often 1, meaning vacuum) and spatially constant but frequency dependent inside the sphere (Fig. 3.1). This yields an expression where the field is an infinite series of spherical harmonics, that can be numerically computed to arbitrary order [57]. The dipolar part gives the polarizability [5]

$$\alpha(\omega) = i\left(\frac{r\omega}{c}\right)^3 \frac{\varepsilon(\omega) - 1}{\varepsilon(\omega) - 2}, \tag{3.4}$$

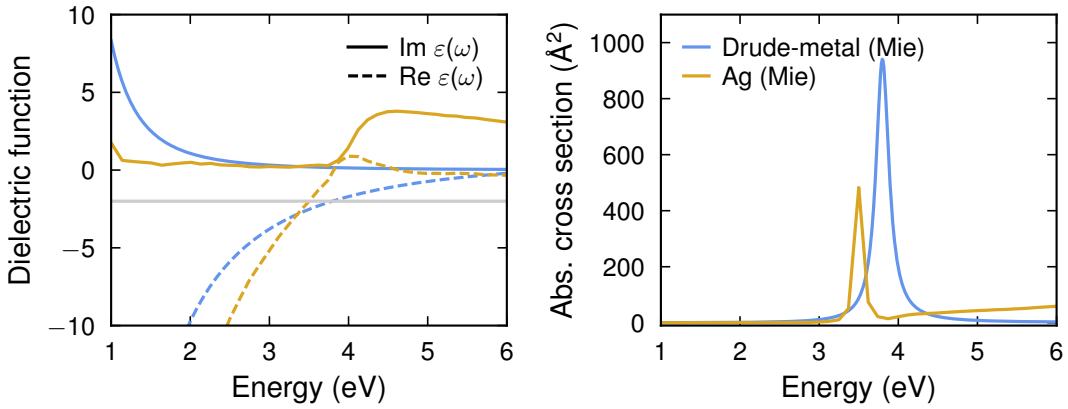

Figure 3.2: Dielectric functions for the Drude metal and experimentally measured for Ag [55]. Using Mie theory, the corresponding absorption cross sections are shown.

where r is the radius of the sphere and c the speed of light. For the Mie sphere, a resonance should appear for frequencies satisfying

$$\text{Re}\,\varepsilon(\omega) = -2, \tag{3.5}$$

assuming that $\varepsilon(\omega)-1$ varies slowly for those frequencies. For the Drude model, this condition is satisfied for $\omega = \sqrt{\omega_p^2/3 - \gamma^2} \approx \omega_p/\sqrt{3}$. The LSPR frequency is approximately the square root of one third of the bulk plasma frequency. Plotting the Mie spectrum using Eq. (3.4) alongside the DF verifies the resonance condition (Fig. 3.2). Here, I have used a sphere of $r = 8\,\text{Å}$ and the Drude parameters $\omega_p = \sqrt{3} \cdot 3.8\,\text{eV}$ and $\gamma = 0.2\,\text{eV}$. A more realistic NP spectrum is obtained by replacing the Drude DF with an experimentally measured DF for Ag [55] (Fig. 3.2). The resonance condition still holds, but the absorption does not decay to zero outside the LSPR peak for Ag. This is because in real materials, electrons can be bound, can be possible to ionize, et cetera , which is reflected in the experimental DF but missing from the very simple DF considered here in the Drude model.

3.2.1 Effect of composition and shape

The noble metals Au and Cu differ from Ag in their dielectric function [55]. Due to higher imaginary parts at the resonance condition, they have much broader LSPRs (Fig. 3.3). Thus different materials can be used to modify optical properties. Furthermore, alloying, that is uniformly mixing materials in the NP interpolates the DFs of the two materials [58, Chapter 4], creating an even larger configurational space. The shape of the NP also impacts the optical response. Extending the Mie theory to ellipsoids, the resonance condition is shifted [58, Chapter 4].

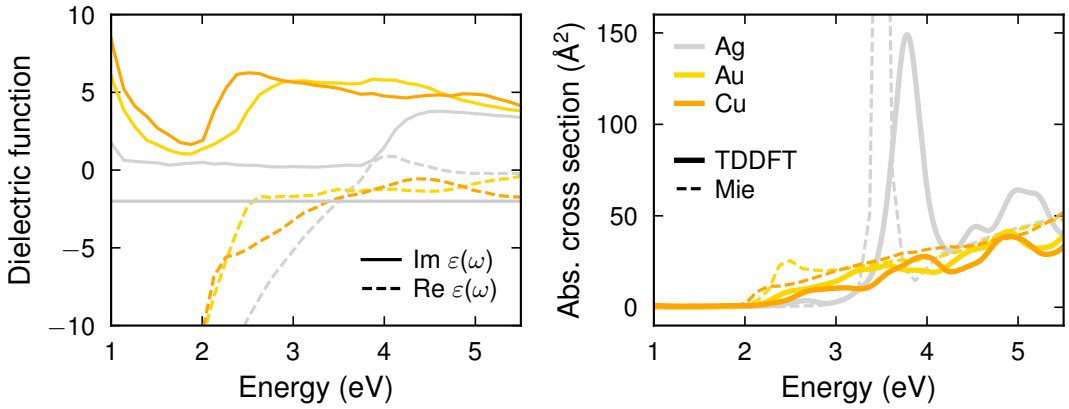

Figure 3.3: Dielectric functions [55] and absorption spectra for small Ag, Au and Cu NPs from TDDFT or Mie theory.

3.2.2 Effect of non-locality

The part of a material near the boundaries of a structure should not be expected to behave in the same way as the material in the bulk, because of the locally different chemical environment. This invalidates the use of a single spatially constant DF for the entire structure. Of course, if the structure is big enough, the difference from the edges would be negligible, so we should expect such models to work worse for smaller particles. This problem can be alleviated by using a non-local DF (i.e., one that has a position, or, equivalently, momentum dependence) [59, Chapter 2]. Corrections for the non-locality predict that the LSPR frequency should be blue-shifted for smaller particles [60]

$$\omega^2_{\mathrm{LSPR}} = \omega^2_{\mathrm{LSPR,Mie}} + \frac{\mathrm{const.}}{r^2}. \tag{3.6}$$

Approximately, the blue-shift is proportional to the inverse of the radius.

3.2.3 Quantum matter description

Using RT-TDDFT, we can readily compute absorption spectra of NPs up to a few hundred atoms in size. The absorption spectra are obtained by self-consistently propagating the time-dependent KS equations under the influence of a δ-kick, as described in Sect. 2.3, for 30 fs. This is enough for the LSP to decay and HCs to form. I used the GPAW code and the GLLB-sc XC functional. The resulting spectra for 201-atom Ag, Au and Cu NPs are shown in Fig. 3.3. In general, the 201-atom NPs (which approximately have a radius of 10 Å) have their resonances at higher energies than their Mie-counterparts. This is because the Mie-theory predicts response in the red-shift limit of Eq. (3.6).

4

Hot-carrier generation and transfer

The absorption of light by a NP excites a LSP resonance that quickly decays into highly energetic, non-thermal electron-hole pairs, usually called hot carriers (HCs). The injection of HCs into molecules and semiconductors is thought to be the driving mechanism in several energy harvesting applications, but it is not fully understood when the injection takes place (immediately as HCs are formed or when they have thermalized?). In this chapter, I discuss the time scales of HC generation in NPs, their energetic distributions, and the processes that eventually lead to their equilibration with the environment. Then I put this in the context of HC transfer to adjacent molecules.

4.1 The time scales of hot-carrier generation

HC formation in NPs is an ultra-fast process. The LSP usually decays within less than 100 fs [61] (even within few tens of fs for small NPs [54, 62, 63]), exciting one electron and leaving a hole behind. Conservation of energy dictates that the energy difference between the electron and hole should equal $\hbar\omega_{\text{photon}}$, meaning that either the electron, or hole, or both, can be considered hot in comparison to the temperature of the environment. As several authors have pointed out [64–66] single electron-hole pairs or distributions thereof are not in thermal equilibrium and a temperature cannot be defined. Nevertheless, the term "hot" is still often used [67]. Furthermore, for illumination intensities corresponding to solar light, the time between LSP excitation events is much longer than their lifetime [65], and there is no initial distribution of HCs, only one excited electron-hole pair. However, when classical EM fields are used in simulations (e.g. in RT-TDDFT) photon absorption is not quantized and fractions of different electron-hole pairs are obtained. These distributions can simply be interpreted as probabilities.

The rate of HC formation is proportional to the sum of states [68]

$$\Gamma_{\text{initial-HC}}(\omega) \sim \sum_{\boldsymbol{k}} \sum_{i}^{\text{occ.}} \sum_{a}^{\text{unocc.}} \left| g_{\text{plasmon},i\boldsymbol{a}\boldsymbol{k}} \right|^2 \cdot \text{Im}\left[\frac{f_{i\boldsymbol{k}} - f_{a\boldsymbol{k}}}{(\varepsilon_{a\boldsymbol{k}} - \varepsilon_{i\boldsymbol{k}}) - \hbar\omega - i\eta} \right], \tag{4.1}$$

where $f_{a\boldsymbol{k}}$, $f_{i\boldsymbol{k}}$, $\varepsilon_{a\boldsymbol{k}}$, and $\varepsilon_{i\boldsymbol{k}}$ are the occupations and eigenenergies of the electron and hole states, η a broadening constant, and $g_{\text{plasmon},i\boldsymbol{a}\boldsymbol{k}}$ a coupling strength of the pair of states $i\boldsymbol{k}, a\boldsymbol{k}$ and the plasmon, proportional to the transition dipole moment. The initial HC distribution will depend on the electronic structure and geometry of the material, as well as the frequency of the exciting light. Theoretical predictions for extended surfaces [68, 69] show two distinct regimes. For $\hbar\omega_{\text{photon}}$ larger than the d-band onset, transitions from the d-band to the sp-band dominate, meaning that the holes are at least as hot as the d-band onset (about 2 eV for Au and Cu) and the electrons relatively cold for optical frequencies. In Ag (d-band onset almost 4 eV) this effect is most extreme, where a single peak in the hot hole (HH) distribution at the d-band, and a corresponding peak just above the Fermi level in the hot electron (HE) distribution, dominate. For $\hbar\omega_{\text{photon}}$ below the d-band onset only sp-intraband transitions are possible, which generally results in broad HC distributions.

In NPs, the momentum $\boldsymbol{k}$ is no longer a good quantum number, and the conservation rules for bulk band structures need not be obeyed. In Ag, excited electrons are in excess on undercoordinated sites on the surface, and this is even more exaggerated for HEs [54]. For very small NPs (< 2 nm), HC distributions in Ag consist of discrete peaks in the entire energy range. With increasing size of NPs, the HC distributions approach that of bulk [54, 70].

The initial non-thermal distribution thermalizes through various scattering processes. A common belief still is that: (1) electron-electron scattering brings the electrons to thermal equilibrium with a much higher temperature than the ionic lattice on a time scale of 100 fs to 1 ps, (2) electron-phonon scattering brings the electronic and ionic temperatures to equilibrium over several ps, and (3) the NP dissipates heat to the environment over 100 ps to 10 ns [61]. However, some predictions put the electron-phonon scattering rates to similar short time scales as electron-electron rates [68]. In either case, to be of any practical use HCs need to be extracted from the material before many electron-electron scattering events, as each event splits the energy of the pairs in roughly half [71].

4.2 Direct versus indirect hot-carrier transfer

There are many demonstrations of HCs being useful for energy harvesting applications. By sandwitching plasmonic NPs between traditional electron- and hole extraction materials, a photovoltaic device can be created [6]. In such a device, HCs are generated due

to the decay of the LSP and rapidly extracted by the corresponding material, to drive a photocurrent. A similar working principle has also been used to extract holes from Au NPs to partake in redox reactions of fuels. The role of the NPs can either be to make the electrically driven reaction selective towards one type of fuel [10], or to drive the reaction without any external bias [9]. There are also plenty of examples of NP-only (no electron or hole-collection materials) plasmonic catalysts of commercially important reactions [8, 11–13, 18, 67, 72]. It is generally thought that orbitals of a reactant molecule are transiently occupied by a HC, which puts the molecule in an excited state [73, 74]. The energy of the excited state is not necessarily high enough to force the chemical reaction of interest, but the reaction barrier is lowered enough to be able to be overcome by thermal vibrations.

Whereas a traditional catalysts lower reaction barriers by ground state hybridization, plasmonic catalysts lower reaction barriers by transiently occupying molecular states after illumination. In both cases, the reaction barrier is commonly overcome by vibrations due to thermal energy.

There are two distinct processes in which HC are thought to be injected to molecules [73]. In indirect HC transfer, HCs are injected after formation [67, 75, 76]. Due to the short lifetimes and mean free paths (few tens of nm [68, 76]) of HCs the window for injection is short in this process. In direct hot-carrier transfer (DHCT) [11, 62, 71, 77] on the other hand, the initial electron-hole pair to be created by the LSP decay consists of one carrier in the NP and the other in the molecule. Catalytic rate experiments generally only measure an increase in rate or selectivity towards certain reactions under illumination, but this does not conclusively reveal which process dominates, or even whether injection takes place at all. Some estimates deem that under continuous illumination the NP will have an increased temperature and the energy deposited in HCs will be much smaller than the energy in the fully thermalized carriers [78]. This has led to a debate [79–83] on the importance of various processes, including traditional thermal catalysis.

The HC distribution that forms in the NP-molecule system immediately after LSP decay, which I call the initial HC distribution, is the quantity relevant for DHCT. If the electrons and holes making up the initial HC distribution are spatially separated by the NP-molecule interface, then they are attributed to the DHCT process. In the next section, I calculate these quantities to find out under which circumstances DHCT is a relevant process.

4.3 Handles for tuning direct transfer

The efficiency of DHCT depends on the energy levels of states (they must be properly aligned with respect to the incoming photons), and the coupling strength of those states to the LSP (Eq. 4.1) through their transition dipole moment. We can expect both of those

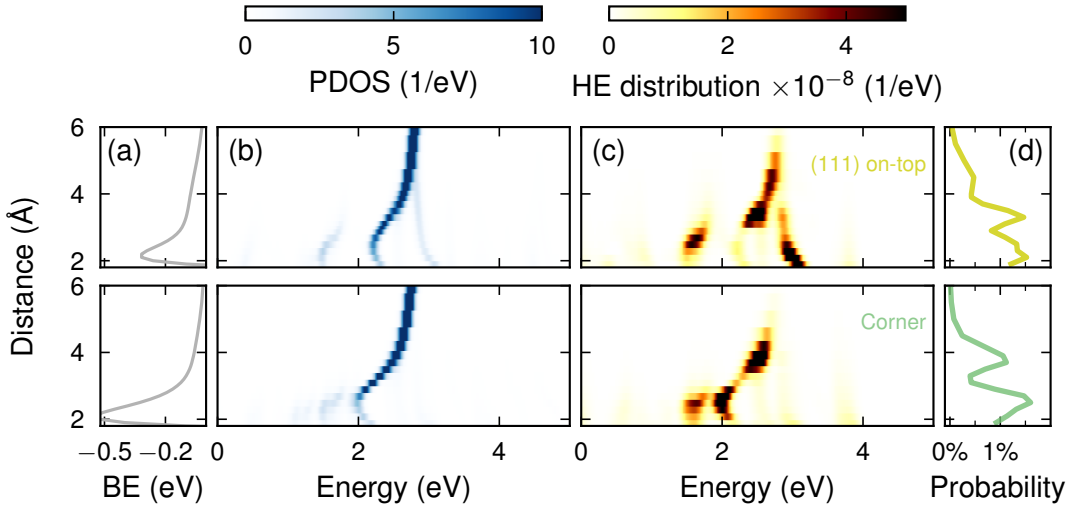

Figure 4.1: In CO approaching the (111 on-top)/corner site on Ag_{201}: (a) binding energy (b) projected density of states (PDOS) (c) HE distribution projected on the molecule and (d) probability of direct electron transfer to CO. HE distributions and transfer probabilities are measured after decay of a 3.8 eV pulse.

to vary as the molecule moves around the NP in a real system. This raises the question: how does the probability of HC transfer depend on position?

In Paper II, we consider a CO molecule in various configurations with respect to an Ag_{201} NP. Specifically, an approach towards high symmetry sites in the middle on a (111) face ((111) on-top site) and on the corner between faces (corner site) is assumed to be representative for this system. We use KS-DFT to find the ground state in each configuration. The binding energy as a function of distance (Fig. 4.1a) confirms that the molecule binds to the NP at distances 2-6 Å, most strongly (hundreds of meV) between approximately 2-3 Å. Mapping out the PDOS of the molecule by distance (Fig. 4.1), we see that the lowest unoccupied molecular orbital (LUMO), starting from 2.8 eV at far distances, shifts downwards by up to 1 eV as the distance is reduced. At distances closer than 3-4 eV, the original LUMO is split into several hybridized states. We should expect these energetic shifts of molecular states to affect the probability of DHCT via the alignment criterion in the denominator in Eq. (4.1).

The system is excited by a 3.8 eV laser pulse (in resonance with the LSP) in a RT-TDDFT framework; the LSP is allowed to decay, and HC distributions are calculated. Projecting the HE distribution on states in the molecule (Fig. 4.1c) we see how the density of HEs varies strongly with distance, and between several hybridized states at each distance. For example, from 3 Å to 4 Å away from the corner site, the LUMO shifts in energy by almost 1 eV, while the number of HEs in the state increases drastically. The increase in HEs contradicts the intuitive idea that transfer should *decrease* with increasing dis-

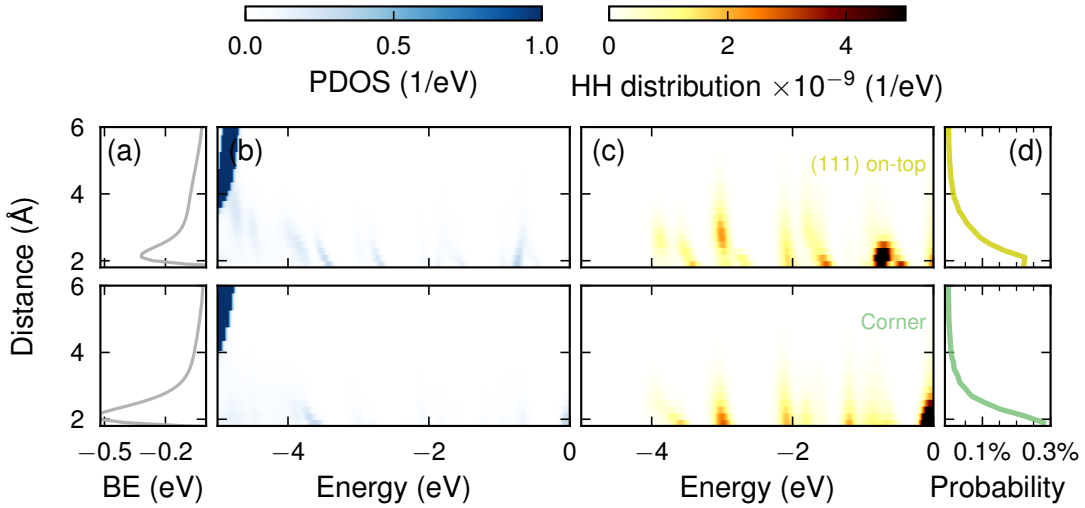

Figure 4.2: In CO approaching the (111 on-top)/corner site on Ag_{201}: (a) binding energy (b) PDOS (c) HH distribution projected on the molecule and (d) probability of direct hole transfer to CO. HE distributions and transfer probabilities are measured after decay of a 3.8 eV pulse. Note the difference in colorbar scale compared to Fig. 4.1.

tance; the increase in transfer is explained by the change in energetic alignment. By shifting in energy, the LUMO aligns to different donor states in the NP, which evidently provide a stronger coupling to the LSP. Another example is that at 2.1 Å from the (111) on-top site, the number of HEs is higher in the 3 eV than in the 1.8 eV LUMO-hybrid state, while at the just slightly larger distance of 2.5 Å, the situation is reversed. Between these two distances, the shifts in LUMO eigenenergy are relatively small, which could suggest that the same donor and molecular states are involved in the transfer, but the coupling strength changes due to changing overlap of the wave functions. The end result of these intricate relations between states is that the probability of DHCT (Fig. 4.1d; obtained by integrating the projected HE distributions and normalizing by the total number of HEs in the NP) varies non-monotonically between 0-2 % for a wide range of distances. The distance dependence of DHCT is sensitive to the site of approach, and DHCT is effective even up to distances of 5 Å.

The transfer of HHs to CO qualitatively differs from the transfer of electrons. The highest occupied molecular orbital (HOMO) is too far below the Fermi level (5 eV) to allow for HH transfer (Fig. 4.2b; binding energies repeated for reference in Fig. 4.2a) and shifts even further away with decreasing distance. Hybridized HOMO states appear at short distances (< 4 Å) which are in range for HH transfer (Fig. 4.2c). Consequently, the probability of HH transfer is at most 0.3 % (Fig. 4.2d; about a factor of 10 less than HE transfer), and exponentially decreasing.

In the alignment criterion Eq. (4.1), the exciting laser frequency acts as a handle deter-

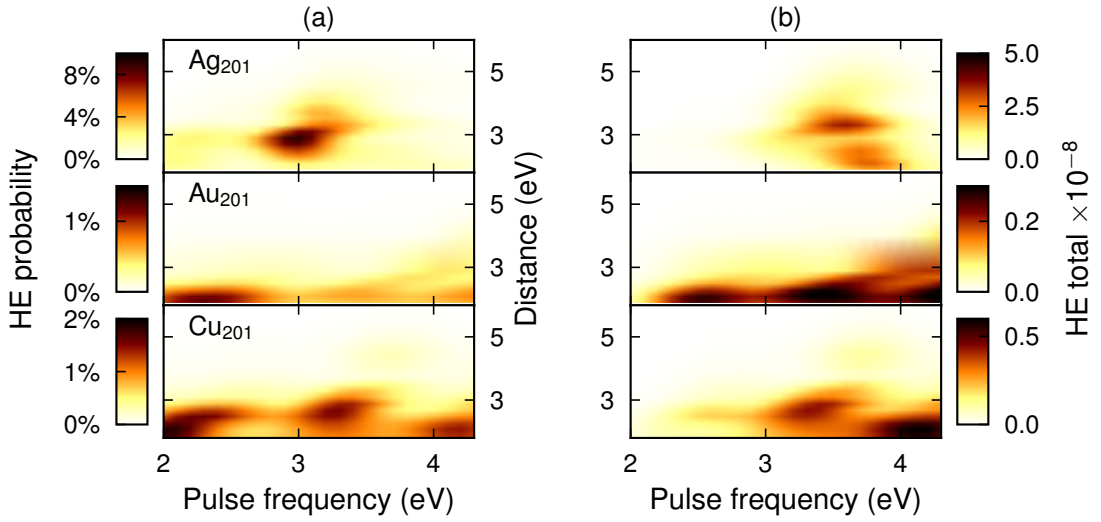

Figure 4.3: HE transfer as a function of distance and pulse frequency for the (111) on-top site. (a) As fraction of all generated carriers. (b) As total number of HEs.

mining the energetic difference between generated electrons and holes. If two strongly coupled electron-hole states are not aligned to the laser frequency at one particular distance, changing the frequency should be able to bring them into alignment. We test this hypothesis by mapping out the relative probability of HE transfer on distance and laser frequency (Fig. 4.3). Indeed, we can enhance the HE transfer probability by reducing the pulse frequency. We also observe that direct HE transfer is effective in Au and Cu NPs, with lower sensitivity of the total number of transferred carrier to the pulse frequency, due to their broader LSPR peaks. For the Ag NP, an increase up to 9 % relative probability of HE transfer can be achieved, at the expense of lower absorption and thus lower total of HEs transferred. The optimum in the total occurs for most distances slightly off the LSPR, at 3.6 eV. This opens the door for further engineering: If the LSPR is also tuned to lower frequencies by changing, e.g., the NP shape, high absorption and high relative transfer probability could be achieved simultaneously.

5 Strong coupling

In the regime of strong light-matter coupling, the behavior of coupled systems is different not only quantitatively, but also qualitatively, from the weakly coupled case. The most sophisticated models of SC belong to the formalism of quantum electrodynamics [19] but the basic ideas are seen already in simple classical models of coupled harmonic oscillators [84]. In this chapter, I explain SC using classical coupled harmonic oscillators, and later present a method that has a detailed description of matter, but the simplest possible EM interactions. For simplicity, Hartree atomic units $e = \hbar = 4\pi\varepsilon_0 = 1$ are used.

5.1 Characteristics of strong coupling

In typical experiments where SC between molecules and light is observed, one takes molecules that have a clearly peaked optical spectrum at ω_0, confines them in an optical cavity, and measures the optical spectrum [85]. The cavity should be tuned so that its resonance frequency is close to ω_0. If SC occurs, the ω_0 peak splits into two peaks (Fig. 5.1). The two peaks correspond to hybrid light-matter states called polaritons, the lower polariton (LP) having frequency $\Omega_- < \omega_0$ and the upper polariton (UP) $\Omega_+ > \omega_0$.

The confinement of the light to a small mode volume inside the cavity is responsible for increasing the strength of the coupling between the molecular transition and the electric field, which is otherwise very weak in the absence of a cavity. In theory, one can imagine turning the coupling strength g between the molecule and the field up from zero to a high value. This is demonstrated later in this chapter. Initially there is an increase in amplitude seen in the spectrum of the molecule (Fig. 5.1). This is known as the Purcell effect and characteristic of *weak* coupling [19]. Eventually the peak splits in two polaritons, a signature of SC, the quantity $\Omega_R = \Omega_+ - \Omega_-$ being known as Rabi splitting.

SC in the context of light and electronic transitions is typically taken to be when the Rabi splitting is larger than the linewidth $\Omega_R > \gamma$ [86].

No matter whether classical matter-classical light, quantum matter-classical light or quantum matter-quantum light models are considered, theory predicts [86]

$$\Omega_R \sim \sqrt{N/V}. \tag{5.1}$$

The certain means for increasing the coupling strength are thus to confine the light to a smaller volume V, and to increase the number of molecules N simultaneously coupling to the cavity.

In quantum models such as the Jaynes-Cummings two-state model [86, 87] g is a direct measure of the coupling strength between the EM field and matter. At resonance of the molecule and cavity, the Rabi splitting is related to g and the linewidths as

$$\Omega_R = \sqrt{4g^2 - (\gamma_{\text{molecule}} - \gamma_{\text{cavity}})^2}. \tag{5.2}$$

The coupling strength is in turn obtained from the transition dipole moment μ and vacuum field strength

$$g = \sqrt{N}\mu E_{\text{vac}} \tag{5.3}$$

$$E_{\text{vac}} = \sqrt{\frac{2\pi\omega_0}{V}}. \tag{5.4}$$

5.2 Coupled harmonic oscillators

The key characteristics of SC can be derived by studying classical coupled harmonic oscillators [84]. Consider the following equation of motion for the position coordinate of a damped harmonic oscillator

$$\ddot{x}(t) + 2\gamma\dot{x}(t) + \omega_0^2 x(t) = C \cdot E(t) \tag{5.5}$$

The oscillator could represent for example a LSP or an electronic transition. This model is even more simplistic than the small sphere of free-electron metal in Chapter 3, but the form can be phenomenologically motivated; the restoring force on the oscillator $\omega_0^2 x(t)$ is proportional to its displacement, the friction $2\gamma\dot{x}(t)$ to its velocity, and C is the coupling strength to the driving field $E(t)$. We can also assume that the oscillator has a dipole that is proportional to the position coordinate with the same strength as the coupling of the electric field to the position

$$d(t) = Cx(t). \tag{5.6}$$

Taking the Fourier transform

$$-\omega^2 x(\omega) + 2i\gamma\omega x(\omega) + \omega_0^2 x(\omega) = C \cdot E(\omega) \tag{5.7}$$

we find the polarizability of the system

$$\alpha(\omega) = \frac{Cx(\omega)}{E(\omega)} = \frac{C^2}{\omega_0^2 - \omega^2 + 2i\omega\gamma}. \tag{5.8}$$

A polarizability of the form Eq. (5.8) is called a Lorentzian, and the corresponding absorption $\omega \cdot \mathrm{Im}\ \alpha$ has a maximum at ω_0 (Fig. 5.1a).

Now, consider two harmonic oscillators 1 and 2 that are coupled through their velocity. The equations of motion are

$$\ddot{x}^{(1)}(t) + 2\gamma_1\dot{x}^{(1)}(t) + \omega_1^2 x^{(1)}(t) + 2g\dot{x}^{(2)}(t) = C_1 \cdot E(t) \tag{5.9}$$

$$\ddot{x}^{(2)}(t) + 2\gamma_2\dot{x}^{(2)}(t) + \omega_2^2 x^{(2)}(t) - 2g\dot{x}^{(1)}(t) = C_2 \cdot E(t), \tag{5.10}$$

The only difference from Eq. (5.5) is the additional coupling of strength $\pm 2g$ to the velocity of the other oscillator. The coupled system needs to be considered to find the solution, which is done conveniently with the tensorial equation

$$\begin{bmatrix} 1 & 0 \\ 0 & 1 \end{bmatrix} \begin{bmatrix} \ddot{x}^{(1)}(t) \\ \ddot{x}^{(2)}(t) \end{bmatrix} + 2 \begin{bmatrix} \gamma_1 & g \\ -g & \gamma_2 \end{bmatrix} \begin{bmatrix} \dot{x}^{(1)}(t) \\ \dot{x}^{(2)}(t) \end{bmatrix} + \begin{bmatrix} \omega_1^2 & 0 \\ 0 & \omega_2^2 \end{bmatrix} \begin{bmatrix} x^{(1)}(t) \\ x^{(2)}(t) \end{bmatrix} = \begin{bmatrix} C_1 \\ C_2 \end{bmatrix} \cdot E(t). \tag{5.11}$$

We take the Fourier transform and introduce the denominators of Lorentzians

$$L_1 = \omega_1^2 - \omega^2 + 2i\omega\gamma_1 \tag{5.12}$$

$$L_2 = \omega_2^2 - \omega^2 + 2i\omega\gamma_2 \tag{5.13}$$

to arrive at

$$\underbrace{\begin{bmatrix} L_1 & 2i\omega g \\ -2i\omega g & L_2 \end{bmatrix}}_{\underline{A}(\omega)} \underbrace{\begin{bmatrix} x^{(1)}(\omega) \\ x^{(2)}(\omega) \end{bmatrix}}_{\underline{x}(\omega)} = \underbrace{\begin{bmatrix} C_1 \\ C_2 \end{bmatrix}}_{\underline{C}} \cdot E(\omega). \tag{5.14}$$

Inverting the tensor $\underline{A}$

$$\underline{A}^{-1}(\omega) = \frac{1}{\det \underline{A}} \begin{bmatrix} L_2 & -2i\omega g \\ 2i\omega g & L_1 \end{bmatrix} \tag{5.15}$$

$$\det \underline{A}(\omega) = L_1 L_2 - 4\omega^2 g^2, \tag{5.16}$$

we obtain the dipoles of both oscillators, the sum of them being the total dipole

$$d(\omega) = \underline{C}^T \begin{bmatrix} x_1(\omega) \\ x_2(\omega) \end{bmatrix} = \underline{C}^T \underline{A}^{-1}(\omega) \underline{C} E(\omega). \tag{5.17}$$

The polarizability of the coupled system is thus

$$\alpha(\omega) = d(\omega)/E(\omega) = \underline{C}^T \underline{A}^{-1}(\omega)\underline{C}. \tag{5.18}$$

Often one of the systems couples much more strongly to the driving field than the other ($C_1 \gg C_2$), for example if oscillator 1 is a cavity and oscillator 2 a small molecule. This motivates setting $C_2 = 0$.

The polarizability of the coupled system, where oscillator 1 couples much more strongly to light than oscillator 2 is

$$\alpha(\omega) = C_1^2 \cdot \frac{L_2}{L_1 L_2 - 4\omega^2 g^2} \tag{5.19a}$$

$$= C_1^2 \cdot \frac{\omega_2^2 - \omega^2 + 2i\omega\gamma_2}{(\omega_1^2 - \omega^2 + 2i\omega\gamma_1)(\omega_2^2 - \omega^2 + 2i\omega\gamma_2) + 4\omega^2 g^2}. \tag{5.19b}$$

If the two oscillators are exactly resonant $\omega_1 = \omega_2 = \omega_0$, we can factorize the determinant

$$\det \underline{A}(\omega) = \left[\omega_0^2 - \omega^2 + i\omega(\gamma_1 + \gamma_2)\right]^2 - \omega^2\left[4g^2 - (\gamma_1 - \gamma_2)^2\right]. \tag{5.20}$$

Let us introduce the notation Ω_R^2 for the bracket in the second term

$$\Omega_R^2 = 4g^2 - (\gamma_1 - \gamma_2). \tag{5.21}$$

and use the identity $a^2 - b^2 = (a - b)(a + b)$ to write the determinant

$$\det \underline{A}(\omega) = L_+ L_-, \tag{5.22}$$

where

$$L_\pm = \left[\omega_0^2 - \omega^2 + \omega(i(\gamma_1 + \gamma_2) \pm \Omega_R)\right]. \tag{5.23}$$

Finally, we multiply and divide the polarizability by $L_+ - L_-$, to cast it into the form

$$\alpha(\omega) = \frac{C_1^2 L_2}{L_+ - L_-} \cdot \frac{L_+ - L_-}{L_+ L_-} \tag{5.24}$$

$$= \frac{C_1^2 L_2}{\omega\Omega_R} \cdot \left(\frac{1}{L_-} - \frac{1}{L_+}\right), \tag{5.25}$$

suggesting that it will, approximately, behave as the difference of $1/L_-$ and $1/L_+$.

At this point, we note that if Ω_R^2 is negative (the coupling strength being smaller than half of the difference in linewidths) then Ω_R is imaginary and consequently $1/L_+$ and

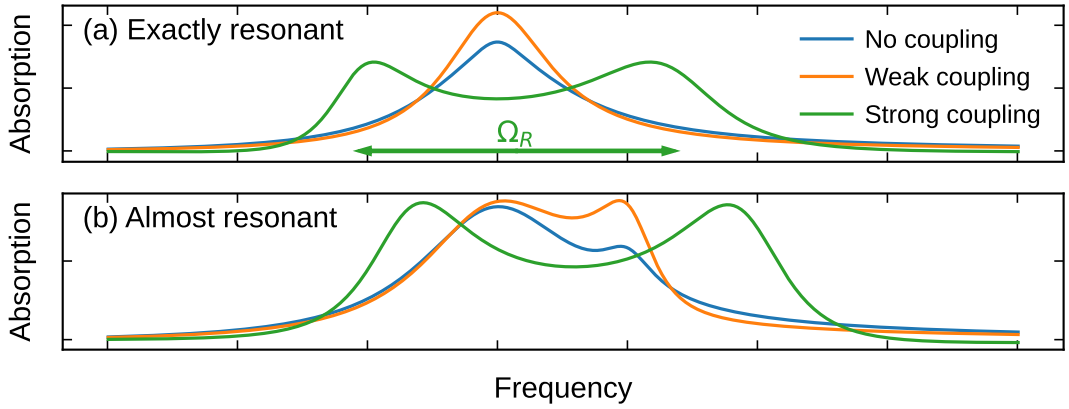

Figure 5.1: Absorption spectrum of uncoupled, weakly coupled and strongly coupled harmonic oscillators in the (a) exactly resonant and (b) almost resonant cases. The almost resonant case shows clearly how the intensity of the higher frequency oscillator, which is small in the uncoupled case, is greatly enhanced for weak coupling (Purcell effect). For SC, Rabi splitting is clearly visible.

$1/L_-$ are Lorentzians with center frequency ω and linewidths $\gamma_1+\gamma_2 \pm \sqrt{4g^2-(\gamma_1-\gamma_2)^2}$. The system is in the weak coupling regime, as the amplitude and width of the spectrum change, but not the frequency (Fig. 5.1). If one the other hand Ω_R^2 is positive, $1/L_+$ and $1/L_-$ are functions similar to Lorentzians, with center frequencies given by

$$\omega = \sqrt{4\omega_0^2 + \frac{\Omega_R^2}{4}} \pm \frac{\Omega_R}{2}. \tag{5.26}$$

Both peaks are thus slightly blueshifted with respect to ω_0, and the peak positions are separated by the Rabi splitting Ω_R (Fig. 5.1).

The classical coupled oscillator model recovers the Rabi splitting expression Eq. (5.2).

5.3 Dipolar coupling

To understand SC in real materials, a detailed description of matter is required. This has been done, for example, using TDDFT [88]. Such an approach is quickly limited by system size, as each electron is explicitly taken into account. SC is known to be able to form polaritonic states delocalized over hundreds of thousands of molecules [19], a size that is unrealistic to model using TDDFT. In Paper I, we apply a method based on dipolar coupling (DC) of subsystems to study SC. The method relies on TDDFT (or other theory) input in the form of polarizabilities of individual subsystems, e.g., molecules and NPs, but is otherwise computationally very cheap even for large ensembles. The goal of the DC method is to find a macroscopic polarizability $\boldsymbol{\alpha}(\omega)$ of the entire ensemble, expressed in the positions and polarizabilities of the individual subsystems. This macroscopic polarizability is defined as the proportionality constant between the external electric field applied to the system and the total dipole of the system

$$\boldsymbol{d}(\omega) = \boldsymbol{\alpha}(\omega)\boldsymbol{E}_{\text{ext}}(\omega). \tag{5.27}$$

In the derivation of the method, we assume that the entire system is contained in a region smaller than the relevant wavelengths of light (hence we neglect retardation effects).

We consider N subsystems enumerated $1, 2, \ldots, N$, referred to as polarizable units, and assume that the only interaction between them is that of interacting point dipoles. Each unit i has a polarizability $\alpha^{(i)}$ that relates the total electric field at the position $\boldsymbol{r}^{(i)}$ of the unit $\boldsymbol{E}^{(i)}_{\text{tot}}(\omega) = \boldsymbol{E}_{\text{tot}}(\boldsymbol{r}^{(i)}, \omega)$ to the dipole of the unit

$$\boldsymbol{d}^{(i)}(\omega) = \boldsymbol{\alpha}^{(i)}(\omega)\boldsymbol{E}^{(i)}_{\text{tot}}(\omega). \tag{5.28}$$

This polarizability encodes all materials properties of the polarizable unit. For simplicity, we have assumed that the units are charge neutral, and have zero dipole moment for zero electric field ($\boldsymbol{d}_{\text{perm}} = 0$). Thus the total dipole moment of the ensemble is obtained by summation

$$\boldsymbol{d}(\omega) = \sum_{i=1}^{N} \boldsymbol{d}^{(i)}(\omega). \tag{5.29}$$

The total electric field at each unit consists of a contribution from an external electric field $\boldsymbol{E}_{\text{ext}}(\omega)$ and the field due to the dipoles of other units. Inserting the distance vector $\boldsymbol{r}^{(ij)} = \boldsymbol{r}^{(i)} - \boldsymbol{r}^{(j)}$ into Eq. (2.14), we obtain the field at the position of unit i due to the dipole of unit j

$$\boldsymbol{T}^{(ij)}\boldsymbol{d}^{(j)}, \tag{5.30}$$

where the coupling is

$$\boldsymbol{T}^{(ij)} = \frac{3\boldsymbol{r}^{(ij)}(\boldsymbol{r}^{(ij)})^{\mathrm{T}}}{\left|\boldsymbol{r}^{(ij)}\right|^5} - \frac{1}{\left|\boldsymbol{r}^{(ij)}\right|^3}. \tag{5.31}$$

This can be summarized by the following equation for the tensors $\underline{d}(\omega)$, $\underline{\alpha}_0(\omega)$, $\underline{E}_{\text{tot}}(\omega)$ and $\underline{E}_{\text{ext}}(\omega)$

$$\underbrace{\begin{bmatrix} \boldsymbol{d}^{(1)}(\omega) \\ \boldsymbol{d}^{(2)}(\omega) \\ \vdots \\ \boldsymbol{d}^{(N)}(\omega) \end{bmatrix}}_{\underline{d}(\omega)} = \underbrace{\begin{bmatrix} \boldsymbol{\alpha}^{(1)}(\omega) & & & \\ & \boldsymbol{\alpha}^{(2)}(\omega) & & \\ & & \ddots & \\ & & & \boldsymbol{\alpha}^{(N)}(\omega) \end{bmatrix}}_{\underline{\alpha}_0(\omega)} \underbrace{\begin{bmatrix} \boldsymbol{E}^{(1)}_{\text{tot}}(\omega) \\ \boldsymbol{E}^{(2)}_{\text{tot}}(\omega) \\ \vdots \\ \boldsymbol{E}^{(N)}_{\text{tot}}(\omega) \end{bmatrix}}_{\underline{E}_{\text{tot}}(\omega)} \tag{5.32}$$

$$\underbrace{\begin{bmatrix} \boldsymbol{E}^{(1)}_{\text{tot}}(\omega) \\ \boldsymbol{E}^{(2)}_{\text{tot}}(\omega) \\ \vdots \\ \boldsymbol{E}^{(N)}_{\text{tot}}(\omega) \end{bmatrix}}_{\underline{E}_{\text{tot}}(\omega)} = \underbrace{\begin{bmatrix} \boldsymbol{E}^{(1)}_{\text{ext}}(\omega) \\ \boldsymbol{E}^{(2)}_{\text{ext}}(\omega) \\ \vdots \\ \boldsymbol{E}^{(N)}_{\text{ext}}(\omega) \end{bmatrix}}_{\underline{E}_{\text{ext}}(\omega)} - \underbrace{\begin{bmatrix} 0 & \boldsymbol{T}_{12} & \dots & \boldsymbol{T}_{1N} \\ \boldsymbol{T}_{21} & 0 & & \boldsymbol{T}_{2N} \\ \vdots & & \ddots & \vdots \\ \boldsymbol{T}_{N1} & \boldsymbol{T}_{N2} & \dots & 0 \end{bmatrix}}_{\underline{T}} \underbrace{\begin{bmatrix} \boldsymbol{d}^{(1)}(\omega) \\ \boldsymbol{d}^{(2)}(\omega) \\ \vdots \\ \boldsymbol{d}^{(N)}(\omega) \end{bmatrix}}_{\underline{d}(\omega)}. \tag{5.33}$$

By substituting Eq. (5.33) into Eq. (5.32) and solving for the induced dipole moment we obtain

$$\underline{d}(\omega) = \left[\underline{I} + \underline{\alpha}_0(\omega)\underline{T}\right]^{-1} \underline{\alpha}_0(\omega)\underline{E}_{\text{ext}}(\omega), \tag{5.34}$$

where $\underline{I}$ is the identity tensor. The proportionality tensor is interpreted as a reducible unit-wise polarizability

$$\underline{\alpha}(\omega) = \left[\underline{I} + \underline{\alpha}_0(\omega)\underline{T}\right]^{-1} \underline{\alpha}_0(\omega) \tag{5.35a}$$

$$= \left[\underline{\alpha}_0(\omega)^{-1} + \underline{T}\right]^{-1}. \tag{5.35b}$$

Having neglected retardation, the external electric field is uniform throughout the system $\boldsymbol{E}_{\text{ext}}(\omega) = \boldsymbol{E}^{(1)}_{\text{ext}}(\omega) = \boldsymbol{E}^{(2)}_{\text{ext}}(\omega) = \ldots = \boldsymbol{E}^{(N)}_{\text{ext}}(\omega)$. The macroscopic polarizability is thus given by the double summation

$$\boldsymbol{\alpha}(\omega) = \sum_{i}^{N} \sum_{j}^{N} [\underline{\alpha}]_{ij}(\omega). \tag{5.36}$$

The computationally most expensive part of the DC method is the inversion Eq. (5.35b), which has to be done once for every frequency of interest.

Using the DC method, we compute the absorption spectrum for a system comprised of an Al_{201} NP and two benzene molecules on each side. The NP has a LSP resonance at 7.7 eV, which is close to the first bright excitation of the molecule at 7.1 eV (using the PBE XC functional). Varying the distance between the molecules effectively modifies

the coupling strength between the molecular excitation and the LSP. This effect is visible in the spectra as increased Rabi splitting of the LP with smaller distances (Fig. 5.2a). Fitting the obtained spectra to the coupled harmonic oscillator model Eq. (5.19b) we see the relationship to the coupling strength directly (Fig. 5.2b). We find that the DC spectra are in good agreement with TDDFT spectra from [88] (Fig. 5.2). The most apparent differences in the spectra are at small distances, where the DC method underestimates the position of the LP. Such a shortcoming is to be expected at short distances, as the method does not allow the systems to hybridize, and neglects charge transfer and near field effects. In contrast to the spectra, the agreement in coupling strength g between TDDFT and DC becomes worse with increasing distance. This can be attributed to two effects: basis set superposition errors associated with localized basis sets in TDDFT lead to a blueshift of the LP at far distances (in turn underestimating g), while the lack of orbital hybridization in DC possibly underestimates g at short distances.

We also vary the number of molecules around the NP (keeping them at the distance of 3 Å). The agreement in spectra (Fig. 5.3a) and coupling strength (Fig. 5.3b) in comparison to the TDDFT data is good. Up to 4 molecules or so, the signature $\sqrt{N}$ dependence of SC is obeyed, and the deviation for more than 4 molecules is the same in DC and TDDFT.

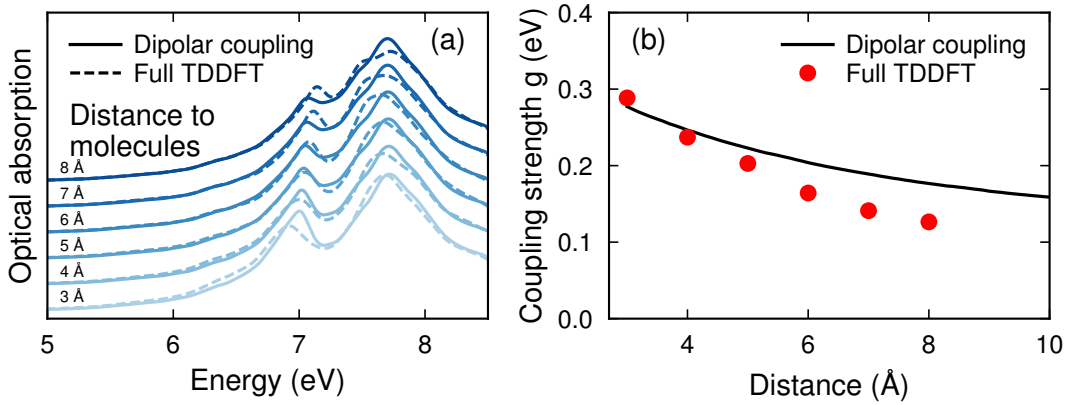

Figure 5.2: (a) Optical spectra for the coupled system of an Al_{201} NP and 2 benzene molecules with different separations to the molecules. The DC data is in good agreement to the reference TDDFT calculations. (b) Coupling strengths obtained by fitting a coupled oscillator model to the DC and TDDFT spectra. SC is achieved for small distances.

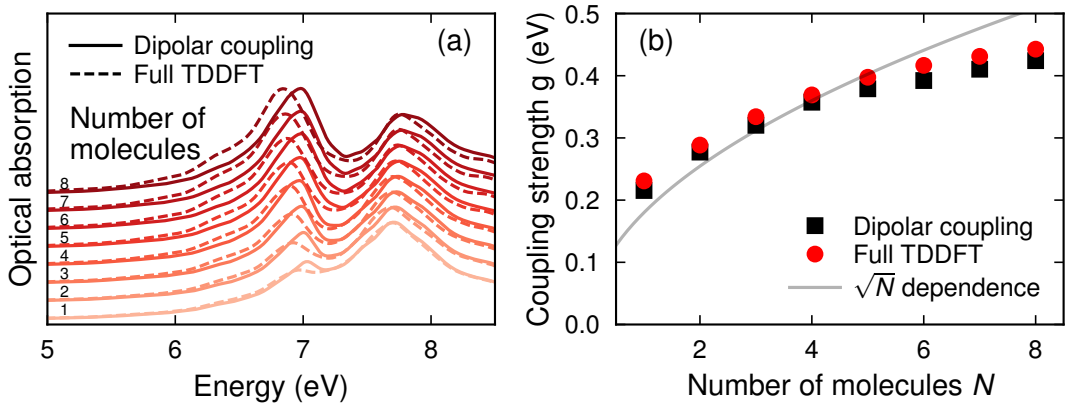

Figure 5.3: (a) Optical spectra for the coupled system of an Al_{201} NP and different numbers of benzene molecules and (b) corresponding coupling strength obtained from fits to a coupled oscillator model. The expected $\sqrt{N}$ dependence is followed for small numbers of molecules, until it saturates. A line is included to guide the eye.

6

Summary of papers

Paper I

Dipolar coupling of nanoparticle-molecule assemblies:
An efficient approach for studying strong coupling

In Paper I we model optical spectra of NP-molecule assemblies as a sets of interacting subsystems, the subsystems each consisting of either a single NP or a single molecule. First, we perform TDDFT calculations for each unique subsystem separately, obtaining

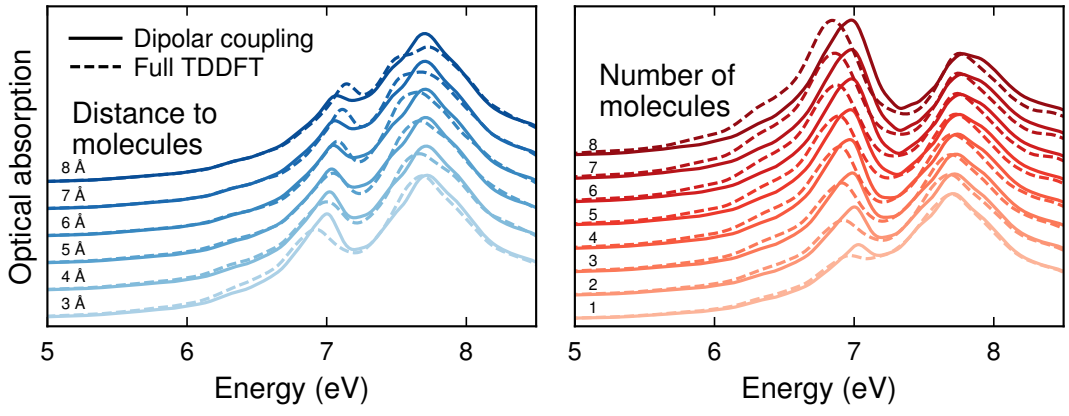

Figure 6.1: Optical spectra calculated for NP-molecule assemblies using our DC method are compared to reference spectra from full TDDFT. The distance of molecules to the plasmonic NP (left) and the number of molecules at a fixed distance (right) are varied.

their individual polarizabilities. Then, we assume that when coupled, the only interaction between subsystems is that of radiating point dipoles, each with the polarizability of the corresponding individual subsystem. We derive a set of equations for the total polarizability of the coupled system, expressed in the positions and polarizabilities of the individual subsystems. This provides a method that has a moderate set-up cost, namely in the computation of individual polarizabilities from TDDFT, but a negligible cost for computing optical spectra for arbitrary assemblies of these units.

We benchmark the accuracy of the dipolar-coupling method against full TDDFT calculations of NP-molecule ensembles where SC occurs. Two distinct peaks corresponding to the LP and UP are visible (Fig. 6.1) and the Rabi splitting, which is a measure of the coupling strength, increases with smaller distance and larger number of molecules. The DC method is in good agreement with TDDFT, except for the position of the LP being underestimated for small distances. This shortcoming is a natural limitation of the DC method, as it does not allow the underlying subsystems to hybridize, and neither does it consider higher-order multipole interactions. In conclusion, the DC method is an efficient method suitable for studying large ensembles of NPs and molecules to a reasonable accuracy, and it is able to capture SC.

Paper II

Hot-Carrier Transfer across a Nanoparticle–Molecule Junction: The Importance of Orbital Hybridization and Level Alignment

In Paper II, we use RT-TDDFT to study the direct HC transfer from a small metal NP to a CO molecule. The transfer process is caused by the decay of the LSP, which we excite with a laser pulse. For a few representative sites of approach, we find the probability of HE transfer to depend non-monotonically on the distance between NP and molecule. The transfer is effective at distances outside the binding energy well (Fig. 6.2; in fact, the *maximum* of HE transfer in some cases occurs outside this region), suggesting that direct HE transfer to gas-phase molecules around the NP can be expected to occur. The probability of HH transfer is, on the other hand, rapidly decaying to zero with increasing distance. Typically, HE transfer is 10 times less likely than HH transfer in this system.

Analyzing the HC transfer in the underlying transitions between KS states, we find the process being very sensitive to the particular pairs of states involved. The HCs generated by the decay of the LSP appear in electron-hole pairs with a difference in eigenenergies equal to the energy of the incoming photon $\hbar\omega$. Thus, for HE transfer, the eigenenergy of the LUMO determines which KS states of the NP can act as donors. With varying distance, the eigenenergy of the LUMO varies (in fact, shifts are visible already beyond the binding energy well), and the condition for available donor states in the NP changes

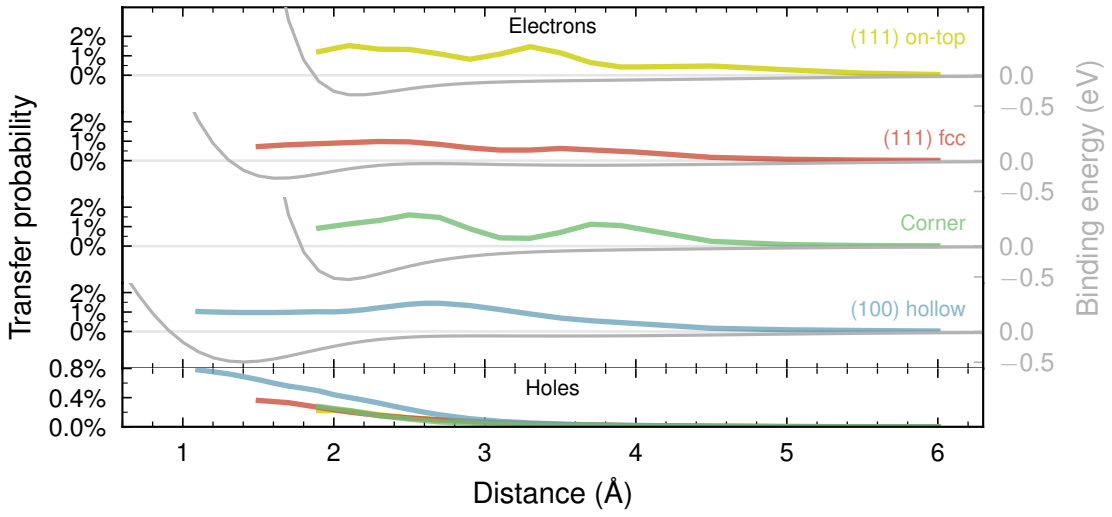

Figure 6.2: Probabilities of HE and HH transfer from Ag_{201} to CO mapped out as a function of distance and site of approach, when excited by a 3.8 eV laser pulse. Binding energies for the system are included in each subpanel.

as well, resulting in a non-monotonic distance dependence of the process probability. For HH transfer the corresponding condition depends on the the HOMO energy. In our system, the HOMO lies further away from the Fermi level than $\hbar\omega$ at far distances, thus prohibiting transfer. At closer distances, HH transfer is non-zero due to the hybridized HOMO having shifted closer to the Fermi level.

In conclusion, the probability of direct HC transfer depends on both ground-state (energetic alignment of KS states) and excited-state (coupling strength between LSP and electron-hole transitions) properties, yielding a complex landscape. The frequency of the exciting laser pulse can be used as a handle for modifying the probabilities.

7 Conclusions and outlook

The aim of this thesis has been to answer the two questions pertaining to the topics of Chapters 4 and 5 respectively:

- What determines the efficiency of hot carrier (HC) transfer from NPs to molecules?
- To what extent is strong coupling (SC) in NP-molecule assemblies captured by dipolar coupling?

In Chapter 4 I have mapped out the initial HC-distribution dependence on the distance and site of approach for a CO molecule approaching noble metal NPs. By projecting the HC distributions on the molecule, I have obtained relative probabilities of direct hot-carrier transfer (DHCT) compared to HC generation in the NP. For the initial HCs, the eigenenergy of the electron minus the eigenenergy of the hole equal the photon energy. The probability of hot electron (HE)/hot hole (HH) transfer thus depends on which occupied/unoccupied states in the NP are allowed to donate/accept an electron to/from the CO LUMO/HOMO, and the coupling strength of those transitions to the localized surface plasmon (LSP). Because the hybridized molecular orbitals shift in energy as the distance is varied, different NP states, with different coupling strengths donate/accept to the NP.

Several microscopic quantities determine the the efficiency of DHCT. The binding energy curve dictates which geometrical configurations of CO-NP are likely. The binding energy curve is influenced by the type of molecule and type of surface [89, 90]. The energetic positions of the hybridized HOMO and LUMO depend on the type of molecule, type of surface, and NP composition. The energetic positions of NP states, i.e., the density of states of the NP, depends on NP composition and size; the latter through formation of atomic-shell-like states in small NPs [91]. For solar or otherwise broadband illumination, the energy of absorbed photons depends on the localized surface plasmon

resonance (LSPR) frequency, which depends on size, shape and composition of the NP, as well its dielectric environment [92]. The coupling strength of electron-hole pairs to the LSP depends on the overlap and orbital angular momentum of states, and the LSP electromagnetic (EM) field mode. In particular, the latter can be greatly enhanced by local geometry of the NP surface [93].

In conclusion, the efficiency of HC transfer depends on the size, shape, composition and environment of the NP, the type of NP surfaces exposed to the molecule, and the type of molecule through the aforementioned relations.

In Chapter 5 I have derived a method to efficiently compute absorption spectra of NP-molecule assemblies based on dipolar coupling (DC). I apply the method to an Al NP surrounded by between 1 and 8 benzene molecules, and compare the results to reference real-time time-dependent density functional theory (RT-TDDFT) calculations for the same system. The agreement between the DC method and the RT-TDDFT results is good, especially in the intermediate distances range. For small distances, there is a quantitative difference in the spectra due to the inherent inability of the DC method to capture charge transfer, orbital hybridization, and multipolar coupling.

The DC method captures SC behavior to the same extent as RT-TDDFT calculations. The behavior includes the $\sqrt{N}$ dependence of the coupling strength on the number of molecules, and the increasing coupling strength with decreasing distance.

7.1 Limitations

Density-functional theory (DFT) is in practice an approximate method due to the need to approximate the exchange-correlation (XC) functional. Better functionals often come with higher computational cost, but even worse: there is no sure way to improve the description of *all* systems with one choice of XC. Often the description of molecules is improved at the expense of metals. The adiabatic approximation of the XC functional in TDDFT is also a limitation, that misses out on electron-electron scattering processes. Since atoms are frozen during the RT-TDDFT calculation, electron-phonon scattering processes are missing as well. This would affect the long-term HC distributions more than the initial, but considering that some estimates put HC lifetimes in the few tens of fs [68] it could affect even the initial HC distributions.

All problems associated with the approximation of the XC functional can in principle be circumvented in the DC method. There is no need to use specifically TDDFT for the input polarizabilities; other theory, or even experimental inputs can be used. However, the DC approximation is quite restrictive, and is only expected to work for well separated systems.

7.2 Outlook

Many questions regarding plasmon mediated HC generation and photocatalysis remain. For energy applications HC generation is not interesting per se; the goal of a complete theoretical model would be to accurately predict photocatalysis rates, i.e. how many chemical reactions per second occur. In the context of TDDFT, this would require properly taking electron-electron (e.g. by a non-adiabatic XC functional) and electron-phonon (by allowing atomic nuclei to move during the simulation) scattering into account. A tremendous increase in simulation time would be necessary to reach the time scales of reactions taking place, and to properly gather statistics. One possible way forward could thus be to train some computationally efficient model on the behavior of the electronic system, and simulate the motion of the nuclei in the framework of this model. E.g. machine learning approaches are gaining popularity for such multiscale modeling [94].

Acknowledgments

I wish to thank Paul Erhart, my main supervisor, for your guidance during this first half of my PhD studies. I really appreciate what I have learned from you about physics, code quality, effective written and oral dissemination of my findings, typesetting, and other more or less useful knowledge. I am also grateful to my assistant supervisors, Tuomas Rossi and Christian Schäfer for your patience with big and small questions, for all fruitful discussions, and for the time you have invested in educating me on TDDFT and the inner workings of GPAW. Thank you all for your help with discussing, proof reading, and editing my papers and thesis.

Thank you, to all past and present members of the CMMT division, who make our workplace a fun and stimulating environment. I can always count on finding someone to discuss anything from compilers to DFT to the best trails for cross country running in Gothenburg.

Finally, I extend my thanks to my friends and family for your encouragement. In particular, thank you to my wife Isabel, for your love and unfailing support.

Bibliography

[1] G. Gao, A. P. O'Mullane, and A. Du, *2D MXenes: A New Family of Promising Catalysts for the Hydrogen Evolution Reaction,* ACS Catalysis **7**, 494 (2017). doi:10.1021/acscatal.6b02754.

[2] C. P. Grey and D. S. Hall, *Prospects for Lithium-Ion Batteries and beyond—a 2030 Vision,* Nature Communications **11**, 6279 (2020). doi:10.1038/s41467-020-19991-4.

[3] Y.-T. Huang, S. R. Kavanagh, D. O. Scanlon, A. Walsh, and R. L. Z. Hoye, *Perovskite-Inspired Materials for Photovoltaics and beyond—from Design to Devices,* Nanotechnology **32**, 132004 (2021). doi:10.1088/1361-6528/abcf6d.

[4] IPCC, *Summary for Policymakers,* in *Climate Change 2022: Mitigation of Climate Change. Contribution of Working Group III to the Sixth Assessment Report of the Intergovernmental Panel on Climate Change*, edited by P. Shukla, J. Skea, R. Slade, A. A. Khourdajie, R. van Diemen, D. McCollum, M. Pathak, S. Some, P. Vyas, R. Fradera, M. Belkacemi, A. Hasija, G. Lisboa, S. Luz, and J. Malley (Cambridge, UK and New York, NY, USA: Cambridge University Press, 2022), p. 3. doi:10.1017/9781009157926.001.

[5] C. F. Bohren, *How Can a Particle Absorb More than the Light Incident on It?,* American Journal of Physics **51**, 323 (1983). doi:10.1119/1.13262.

[6] X. Geng, M. Abdellah, R. Bericat Vadell, M. Folkenant, T. Edvinsson, and J. Sá, *Direct Plasmonic Solar Cell Efficiency Dependence on Spiro-OMeTAD Li-TFSI Content,* Nanomaterials **11**, 3329 (2021). doi:10.3390/nano11123329.

[7] J. S. DuChene, G. Tagliabue, A. J. Welch, X. Li, W.-H. Cheng, and H. A. Atwater, *Optical Excitation of a Nanoparticle Cu/p-NiO Photocathode Improves Reaction Selectivity for CO2 Reduction in Aqueous Electrolytes,* Nano Letters **20**, 2348 (2020). doi:10.1021/acs.nanolett.9b04895.

[8] U. Aslam, V. G. Rao, S. Chavez, and S. Linic, *Catalytic Conversion of Solar to Chemical Energy on Plasmonic Metal Nanostructures,* Nature Catalysis **1**, 656 (2018). doi:10.1038/s41929-018-0138-x.

[9] R. Li, W.-H. Cheng, M. H. Richter, J. S. DuChene, W. Tian, C. Li, and H. A. Atwater, *Unassisted Highly Selective Gas-Phase CO2 Reduction with a Plasmonic Au/p-GaN Photocatalyst Using H2O as an Electron Donor,* ACS Energy Letters **6**, 1849 (2021). doi:10.1021/acsenergylett.1c00392.

[10] J. S. DuChene, G. Tagliabue, A. J. Welch, W.-H. Cheng, and H. A. Atwater, *Hot Hole Collection and Photoelectrochemical CO2 Reduction with Plasmonic Au/p-GaN Photocathodes,* Nano Letters **18**, 2545 (2018). doi:10.1021/acs.nanolett.8b00241.

[11] P. Christopher, H. Xin, and S. Linic, *Visible-Light-Enhanced Catalytic Oxidation Reactions on Plasmonic Silver Nanostructures,* Nature Chemistry **3**, 467 (2011). doi:10.1038/nchem.1032.

[12] T. Hou, L. Chen, Y. Xin, W. Zhu, C. Zhang, W. Zhang, S. Liang, and L. Wang, *Porous CuFe for Plasmon-Assisted N2 Photofixation,* ACS Energy Letters **5**, 2444 (2020). doi:10.1021/acsenergylett.0c00959.

[13] Y. Yamazaki, Y. Kuwahara, K. Mori, T. Kamegawa, and H. Yamashita, *Enhanced Catalysis of Plasmonic Silver Nanoparticles by a Combination of Macro-/Mesoporous Nanostructured Silica Support,* The Journal of Physical Chemistry C **125**, 9150 (2021). doi:10.1021/acs.jpcc.1c01669.

[14] P. Zhao, N. Li, and D. Astruc, *State of the Art in Gold Nanoparticle Synthesis,* Coordination Chemistry Reviews **257**, 638 (2013). doi:10.1016/j.ccr.2012.09.002.

[15] M. Grzelczak, J. Pérez-Juste, P. Mulvaney, and L. M. Liz-Marzán, *Shape Control in Gold Nanoparticle Synthesis,* Chemical Society Reviews **37**, 1783 (2008). doi:10.1039/B711490G.

[16] F. Negreiros, L. Sementa, G. Barcaro, I. Fechete, L. Piccolo, and A. Fortunelli, *Chapter 8 - Reactivity and Catalysis by Nanoalloys,* in *Nanoalloys (Second Edition)*, edited by F. Calvo (Oxford: Elsevier, 2020), p. 267. doi:10.1016/B978-0-12-819847-6.00014-0.

[17] U. Aslam and S. Linic, *Addressing Challenges and Scalability in the Synthesis of Thin Uniform Metal Shells on Large Metal Nanoparticle Cores: Case Study of Ag–Pt Core–Shell Nanocubes,* ACS Applied Materials & Interfaces **9**, 43127 (2017). doi:10.1021/acsami.7b14474.

[18] H. Ren, J.-L. Yang, W.-M. Yang, H.-L. Zhong, J.-S. Lin, P. M. Radjenovic, L. Sun, H. Zhang, J. Xu, Z.-Q. Tian, and J.-F. Li, *Core–Shell–Satellite Plasmonic Photocatalyst for Broad-Spectrum Photocatalytic Water Splitting,* ACS Materials Letters **3**, 69 (2021). doi:10.1021/acsmaterialslett.0c00479.

[19] T. W. Ebbesen, *Hybrid Light–Matter States in a Molecular and Material Science Perspective,* Accounts of Chemical Research **49**, 2403 (2016). doi:10.1021/acs.accounts.6b00295.

[20] J. A. Hutchison, T. Schwartz, C. Genet, E. Devaux, and T. W. Ebbesen, *Modifying Chemical Landscapes by Coupling to Vacuum Fields,* Angewandte Chemie International Edition **51**, 1592 (2012). doi:10.1002/anie.201107033.

[21] J. J. Mortensen, L. B. Hansen, and K. W. Jacobsen, *Real-Space Grid Implementation of the Projector Augmented Wave Method,* Physical Review B **71**, 035109 (2005). doi:10.1103/PhysRevB.71.035109.

[22] J. Enkovaara, C. Rostgaard, J. J. Mortensen, J. Chen, M. Dułak, L. Ferrighi, J. Gavnholt, C. Glinsvad, V. Haikola, H. A. Hansen, H. H. Kristoffersen, M. Kuisma, A. H. Larsen, L. Lehtovaara, M. Ljungberg, O. Lopez-Acevedo, P. G. Moses, J. Ojanen, T. Olsen, V. Petzold, N. A. Romero, J. Stausholm-Møller, M. Strange, G. A. Tritsaris, M. Vanin, M. Walter, B. Hammer, H. Häkkinen, G. K. H. Madsen, R. M. Nieminen, J. K. Nørskov, M. Puska, T. T. Rantala, J. Schiøtz, K. S. Thygesen, and K. W. Jacobsen, *Electronic Structure Calculations with GPAW: A Real-Space Implementation of the Projector Augmented-Wave Method,* Journal of Physics: Condensed Matter **22**, 253202 (2010). doi:10.1088/0953-8984/22/25/253202.

[23] A. H. Larsen, M. Vanin, J. J. Mortensen, K. S. Thygesen, and K. W. Jacobsen, *Localized Atomic Basis Set in the Projector Augmented Wave Method,* Physical Review B **80**, 195112 (2009). doi:10.1103/PhysRevB.80.195112.

[24] M. Kuisma, A. Sakko, T. P. Rossi, A. H. Larsen, J. Enkovaara, L. Lehtovaara, and T. T. Rantala, *Localized Surface Plasmon Resonance in Silver Nanoparticles: Atomistic First-Principles*

Time-Dependent Density-Functional Theory Calculations, Physical Review B **91**, 115431 (2015). doi:10.1103/PhysRevB.91.115431.

[25] M. Kuisma, J. Ojanen, J. Enkovaara, and T. T. Rantala, *Kohn-Sham Potential with Discontinuity for Band Gap Materials,* Physical Review B **82**, 115106 (2010). doi:10.1103/PhysRevB.82.115106.

[26] T. P. Rossi, M. Kuisma, M. J. Puska, R. M. Nieminen, and P. Erhart, *Kohn–Sham Decomposition in Real-Time Time-Dependent Density-Functional Theory: An Efficient Tool for Analyzing Plasmonic Excitations,* Journal of Chemical Theory and Computation **13**, 4779 (2017). doi:10.1021/acs.jctc.7b00589.

[27] A. H. Larsen, J. J. Mortensen, J. Blomqvist, I. E. Castelli, R. Christensen, M. Du\lak, J. Friis, M. N. Groves, B. Hammer, C. Hargus, E. D. Hermes, P. C. Jennings, P. B. Jensen, J. Kermode, J. R. Kitchin, E. L. Kolsbjerg, J. Kubal, K. Kaasbjerg, S. Lysgaard, J. B. Maronsson, T. Maxson, T. Olsen, L. Pastewka, A. Peterson, C. Rostgaard, J. Schiøtz, O. Schütt, M. Strange, K. S. Thygesen, T. Vegge, L. Vilhelmsen, M. Walter, Z. Zeng, and K. W. Jacobsen, *The Atomic Simulation Environment—a Python Library for Working with Atoms,* Journal of Physics: Condensed Matter **29**, 273002 (2017). doi:10.1088/1361-648X/aa680e.

[28] G. Kresse and J. Hafner, *Ab Initio Molecular Dynamics for Liquid Metals,* Physical Review B **47**, 558 (1993). doi:10.1103/PhysRevB.47.558.

[29] G. Kresse and J. Furthmüller, *Efficient Iterative Schemes for Ab Initio Total-Energy Calculations Using a Plane-Wave Basis Set,* Physical Review B **54**, 11169 (1996). doi:10.1103/PhysRevB.54.11169.

[30] G. Kresse and J. Furthmüller, *Efficiency of Ab-Initio Total Energy Calculations for Metals and Semiconductors Using a Plane-Wave Basis Set,* Computational Materials Science **6**, 15 (1996). doi:10.1016/0927-0256(96)00008-0.

[31] G. Kresse and D. Joubert, *From Ultrasoft Pseudopotentials to the Projector Augmented-Wave Method,* Physical Review B **59**, 1758 (1999). doi:10.1103/PhysRevB.59.1758.

[32] D. J. Griffiths, *Introduction to Electrodynamics* (Upper Saddle River, NJ: Pearson, 1998).

[33] L. D. Landau, E. M. Lifshitz, and L. P. Pitaevskii, *Electrodynamics of Continuous Media* (Oxford, England: Butterworth-Heinemann, 1984).

[34] H. C. van der Hulst, *Light Scattering by Small Particles* (Mineola, NY: Dover Publications, 1981).

[35] M. Born and R. Oppenheimer, *Zur Quantentheorie Der Molekeln,* Annalen der Physik **389**, 457 (1927). doi:10.1002/andp.19273892002.

[36] R. M. Martin, *Electronic Structure: Basic Theory and Practical Methods* (Cambridge University Press, 2004). ISBN 978-0-521-53440-6 978-0-521-78285-2 978-0-511-80576-9. doi:10.1017/CBO9780511805769.

[37] W. Kohn, *Nobel Lecture: Electronic Structure of Matter—Wave Functions and Density Functionals,* Reviews of Modern Physics **71**, 1253 (1999). doi:10.1103/RevModPhys.71.1253.

[38] P. Hohenberg and W. Kohn, *Inhomogeneous Electron Gas,* Physical Review **136**, B864 (1964). doi:10.1103/PhysRev.136.B864.

[39] W. Kohn and L. J. Sham, *Self-Consistent Equations Including Exchange and Correlation Effects,* Physical Review **140**, A1133 (1965). doi:10.1103/PhysRev.140.A1133.

[40] C. A. Ullrich, *Review of Ground-State Density-Functional Theory,* in *Time-Dependent Density-Functional Theory* (Oxford University Press, 2011), p. 10.

[41] P. A. M. Dirac, *Note on Exchange Phenomena in the Thomas Atom,* Mathematical Proceedings of the Cambridge Philosophical Society **26**, 376 (1930). doi:10.1017/S0305004100016108.

[42] F. Bloch, *Bemerkung zur Elektronentheorie des Ferromagnetismus und der elektrischen Leitfähigkeit,* Zeitschrift für Physik **57**, 545 (1929). doi:10.1007/BF01340281.

[43] J. P. Perdew and A. Zunger, *Self-Interaction Correction to Density-Functional Approximations for Many-Electron Systems,* Physical Review B **23**, 5048 (1981). doi:10.1103/PhysRevB.23.5048.

[44] J. P. Perdew, K. Burke, and M. Ernzerhof, *Generalized Gradient Approximation Made Simple,* Physical Review Letters **77**, 3865 (1996). doi:10.1103/PhysRevLett.77.3865.

[45] O. Gritsenko, R. van Leeuwen, E. van Lenthe, and E. J. Baerends, *Self-Consistent Approximation to the Kohn-Sham Exchange Potential,* Physical Review A **51**, 1944 (1995). doi:10.1103/PhysRevA.51.1944.

[46] J. P. Perdew and M. Levy, *Physical Content of the Exact Kohn-Sham Orbital Energies: Band Gaps and Derivative Discontinuities,* Physical Review Letters **51**, 1884 (1983). doi:10.1103/PhysRevLett.51.1884.

[47] J. Yan, K. W. Jacobsen, and K. S. Thygesen, *First-Principles Study of Surface Plasmons on Ag(111) and H/Ag(111),* Physical Review B **84**, 235430 (2011). doi:10.1103/PhysRevB.84.235430.

[48] J. Yan, K. W. Jacobsen, and K. S. Thygesen, *Conventional and Acoustic Surface Plasmons on Noble Metal Surfaces: A Time-Dependent Density Functional Theory Study,* Physical Review B **86**, 241404 (2012). doi:10.1103/PhysRevB.86.241404.

[49] E. Runge and E. K. U. Gross, *Density-Functional Theory for Time-Dependent Systems,* Physical Review Letters **52**, 997 (1984). doi:10.1103/PhysRevLett.52.997.

[50] R. van Leeuwen, *Mapping from Densities to Potentials in Time-Dependent Density-Functional Theory,* Physical Review Letters **82**, 3863 (1999). doi:10.1103/PhysRevLett.82.3863.

[51] M. E. Casida, *Time-Dependent Density-Functional Theory for Molecules and Molecular Solids,* Journal of Molecular Structure: THEOCHEM **914**, 3 (2009). doi:10.1016/j.theochem.2009.08.018.

[52] I. Vasiliev, S. Öğüt, and J. R. Chelikowsky, Ab Initio *Excitation Spectra and Collective Electronic Response in Atoms and Clusters,* Physical Review Letters **82**, 1919 (1999). doi:10.1103/PhysRevLett.82.1919.

[53] I. Vasiliev, S. Öğüt, and J. R. Chelikowsky, *First-Principles Density-Functional Calculations for Optical Spectra of Clusters and Nanocrystals,* Physical Review B **65**, 115416 (2002). doi:10.1103/PhysRevB.65.115416.

[54] T. P. Rossi, P. Erhart, and M. Kuisma, *Hot-Carrier Generation in Plasmonic Nanoparticles: The Importance of Atomic Structure,* ACS Nano **14**, 9963 (2020). doi:10.1021/acsnano.0c03004.

[55] P. B. Johnson and R. W. Christy, *Optical Constants of the Noble Metals,* Physical Review B **6**, 4370 (1972). doi:10.1103/PhysRevB.6.4370.

[56] G. Mie, *Beiträge Zur Optik Trüber Medien, Speziell Kolloidaler Metallösungen,* Annalen der Physik **330**, 377 (1908). doi:10.1002/andp.19083300302.

[57] K. Ladutenko, U. Pal, A. Rivera, and O. Peña-Rodríguez, *Mie Calculation of Electromagnetic Near-Field for a Multilayered Sphere,* Computer Physics Communications **214**, 225 (2017). doi:10.1016/j.cpc.2017.01.017.

[58] M. Rahm, *There Is an Alloy at the End of the Rainbow: Structure and Optical Properties From Bulk to Nano*. PhD thesis, Chalmers University of Technology, 2021.

[59] T. Rossi, *Computational Modeling of Quantum Aspects in Plasmonic Nanostructures* (Aalto University, 2017). ISBN 978-952-60-7586-0.

[60] S. Raza, W. Yan, N. Stenger, M. Wubs, and N. A. Mortensen, *Blueshift of the Surface Plasmon Resonance in Silver Nanoparticles: Substrate Effects,* Optics Express **21**, 27344 (2013). doi:10.1364/OE.21.027344.

[61] M. L. Brongersma, N. J. Halas, and P. Nordlander, *Plasmon-Induced Hot Carrier Science and Technology,* Nature Nanotechnology **10**, 25 (2015). doi:10.1038/nnano.2014.311.

[62] P. V. Kumar, T. P. Rossi, D. Marti-Dafcik, D. Reichmuth, M. Kuisma, P. Erhart, M. J. Puska, and D. J. Norris, *Plasmon-Induced Direct Hot-Carrier Transfer at Metal–Acceptor Interfaces,* ACS Nano **13**, 3188 (2019). doi:10.1021/acsnano.8b08703.

[63] J. Ma and S. Gao, *Plasmon-Induced Electron–Hole Separation at the Ag/TiO_2 (110) Interface,* ACS Nano **13**, 13658 (2019). doi:10.1021/acsnano.9b03555.

[64] J. B. Khurgin, *Hot Carriers Generated by Plasmons: Where Are They Generated and Where Do They Go from There?,* Faraday Discussions **214**, 35 (2019). doi:10.1039/C8FD00200B.

[65] J. B. Khurgin, *Fundamental Limits of Hot Carrier Injection from Metal in Nanoplasmonics,* Nanophotonics **9**, 453 (2020). doi:10.1515/nanoph-2019-0396.

[66] Y. Sivan and Y. Dubi, *Theory of "Hot" Photoluminescence from Drude Metals,* ACS Nano **15**, 8724 (2021). doi:10.1021/acsnano.1c00835.

[67] L. Zhou, M. Lou, J. L. Bao, C. Zhang, J. G. Liu, J. M. P. Martirez, S. Tian, L. Yuan, D. F. Swearer, H. Robatjazi, E. A. Carter, P. Nordlander, and N. J. Halas, *Hot Carrier Multiplication in Plasmonic Photocatalysis,* Proceedings of the National Academy of Sciences **118**, e2022109118 (2021). doi:10.1073/pnas.2022109118.

[68] M. Bernardi, J. Mustafa, J. B. Neaton, and S. G. Louie, *Theory and Computation of Hot Carriers Generated by Surface Plasmon Polaritons in Noble Metals,* Nature Communications **6**, 7044 (2015). doi:10.1038/ncomms8044.

[69] R. Sundararaman, P. Narang, A. S. Jermyn, W. A. Goddard III, and H. A. Atwater, *Theoretical Predictions for Hot-Carrier Generation from Surface Plasmon Decay,* Nature Communications **5**, 5788 (2014). doi:10.1038/ncomms6788.

[70] H. Jin, J. M. Kahk, D. A. Papaconstantopoulos, A. Ferreira, and J. Lischner, *Plasmon-Induced Hot Carriers from Interband and Intraband Transitions in Large Noble Metal Nanoparticles,* PRX Energy **1**, 013006 (2022). doi:10.1103/PRXEnergy.1.013006.

[71] J. B. Khurgin, A. Petrov, M. Eich, and A. V. Uskov, *Direct Plasmonic Excitation of the Hybridized Surface States in Metal Nanoparticles,* ACS Photonics **8**, 2041 (2021). doi:10.1021/acsphotonics.1c00167.

[72] U. Aslam, S. Chavez, and S. Linic, *Controlling Energy Flow in Multimetallic Nanostructures for Plasmonic Catalysis,* Nature Nanotechnology **12**, 1000 (2017). doi:10.1038/nnano.2017.131.

[73] S. Linic, U. Aslam, C. Boerigter, and M. Morabito, *Photochemical Transformations on Plasmonic Metal Nanoparticles,* Nature Materials **14**, 567 (2015). doi:10.1038/nmat4281.

[74] S. Mukherjee, F. Libisch, N. Large, O. Neumann, L. V. Brown, J. Cheng, J. B. Lassiter, E. A. Carter, P. Nordlander, and N. J. Halas, *Hot Electrons Do the Impossible: Plasmon-Induced Dissociation of H2 on Au,* Nano Letters **13**, 240 (2013). doi:10.1021/nl303940z.

[75] B. Seemala, A. J. Therrien, M. Lou, K. Li, J. P. Finzel, J. Qi, P. Nordlander, and P. Christopher, *Plasmon-Mediated Catalytic O2 Dissociation on Ag Nanostructures: Hot Electrons or Near Fields?,* ACS Energy Letters **4**, 1803 (2019). doi:10.1021/acsenergylett.9b00990.

[76] S.-C. Huang, X. Wang, Q.-Q. Zhao, J.-F. Zhu, C.-W. Li, Y.-H. He, S. Hu, M. M. Sartin, S. Yan, and B. Ren, *Probing Nanoscale Spatial Distribution of Plasmonically Excited Hot Carriers,* Nature Communications **11**, 4211 (2020). doi:10.1038/s41467-020-18016-4.

[77] P. V. Kumar, T. P. Rossi, M. Kuisma, P. Erhart, and D. J. Norris, *Direct Hot-Carrier Transfer in Plasmonic Catalysis,* Faraday Discussions **214**, 189 (2019). doi:10.1039/C8FD00154E.

[78] Y. Dubi and Y. Sivan, *"Hot" Electrons in Metallic Nanostructures—Non-Thermal Carriers or Heating?,* Light: Science & Applications **8**, 89 (2019). doi:10.1038/s41377-019-0199-x.

[79] Y. Dubi, I. W. Un, and Y. Sivan, *Thermal Effects – an Alternative Mechanism for Plasmon-Assisted Photocatalysis,* Chemical Science **11**, 5017 (2020). doi:10.1039/C9SC06480J.

[80] P. K. Jain, *Comment on "Thermal Effects – an Alternative Mechanism for Plasmon-Assisted Photocatalysis" by Y. Dubi, I. W. Un and Y. Sivan, Chem. Sci. , 2020, 11 , 5017,* Chemical Science **11**, 9022 (2020). doi:10.1039/D0SC02914A.

[81] L. Zhou, D. F. Swearer, C. Zhang, H. Robatjazi, H. Zhao, L. Henderson, L. Dong, P. Christopher, E. A. Carter, P. Nordlander, and N. J. Halas, *Quantifying Hot Carrier and Thermal Contributions in Plasmonic Photocatalysis,* Science **362**, 69 (2018). doi:10.1126/science.aat6967.

[82] Y. Sivan, J. Baraban, I. W. Un, and Y. Dubi, *Comment on "Quantifying Hot Carrier and Thermal Contributions in Plasmonic Photocatalysis",* Science **364**, eaaw9367 (2019). doi:10.1126/science.aaw9367.

[83] L. Zhou, D. F. Swearer, H. Robatjazi, A. Alabastri, P. Christopher, E. A. Carter, P. Nordlander, and N. J. Halas, *Response to Comment on "Quantifying Hot Carrier and Thermal Contributions in Plasmonic Photocatalysis",* Science **364**, eaaw9545 (2019). doi:10.1126/science.aaw9545.

[84] X. Wu, S. K. Gray, and M. Pelton, *Quantum-Dot-Induced Transparency in a Nanoscale Plasmonic Resonator,* Optics Express **18**, 23633 (2010). doi:10.1364/OE.18.023633.

[85] T. Schwartz, J. A. Hutchison, J. Léonard, C. Genet, S. Haacke, and T. W. Ebbesen, *Polariton Dynamics under Strong Light–Molecule Coupling,* ChemPhysChem **14**, 125 (2013). doi:10.1002/cphc.201200734.

[86] P. Törmä and W. L. Barnes, *Strong Coupling between Surface Plasmon Polaritons and Emitters: A Review,* Reports on Progress in Physics **78**, 013901 (2014). doi:10.1088/0034-4885/78/1/013901.

[87] E. Jaynes and F. Cummings, *Comparison of Quantum and Semiclassical Radiation Theories with Application to the Beam Maser,* Proceedings of the IEEE **51**, 89 (1963). doi:10.1109/PROC.1963.1664.

[88] T. P. Rossi, T. Shegai, P. Erhart, and T. J. Antosiewicz, *Strong Plasmon-Molecule Coupling at the Nanoscale Revealed by First-Principles Modeling,* Nature Communications **10**, 3336 (2019). doi:10.1038/s41467-019-11315-5.

[89] M. Gajdo, A. Eichler, and J. Hafner, *CO Adsorption on Close-Packed Transition and Noble Metal Surfaces: Trends from* Ab Initio *Calculations,* Journal of Physics: Condensed Matter **16**, 1141 (2004). doi:10.1088/0953-8984/16/8/001.

[90] B. W. J. Chen, D. Kirvassilis, Y. Bai, and M. Mavrikakis, *Atomic and Molecular Adsorption on Ag(111),* The Journal of Physical Chemistry C **123**, 7551 (2019). doi:10.1021/acs.jpcc.7b11629.

[91] A. H. Larsen, J. Kleis, K. S. Thygesen, J. K. Nørskov, and K. W. Jacobsen, *Electronic Shell Structure and Chemisorption on Gold Nanoparticles,* Physical Review B **84**, 245429 (2011). doi:10.1103/PhysRevB.84.245429.

[92] L. Román Castellanos, O. Hess, and J. Lischner, *Dielectric Engineering of Hot-Carrier Generation by Quantized Plasmons in Embedded Silver Nanoparticles,* The Journal of Physical Chemistry C **125**, 3081 (2021). doi:10.1021/acs.jpcc.0c07617.

[93] F. Benz, M. K. Schmidt, A. Dreismann, R. Chikkaraddy, Y. Zhang, A. Demetriadou, C. Carnegie, H. Ohadi, B. de Nijs, R. Esteban, J. Aizpurua, and J. J. Baumberg, *Single-Molecule Optomechanics in "Picocavities",* Science **354**, 726 (2016). doi:10.1126/science.aah5243.

[94] A. P. Bartók, S. De, C. Poelking, N. Bernstein, J. R. Kermode, G. Csányi, and M. Ceriotti, *Machine Learning Unifies the Modeling of Materials and Molecules,* Science Advances **3**, e1701816 (2017). doi:10.1126/sciadv.1701816.